Hydration mechanisms in Roman seawater concrete: Archaeological analogue for validation of long-term ageing reactive transport model

Fructueux Jesugnon Sohounme, Mejdi Neji, Nicolas Seigneur, Katia Schörle, Arnaud Coutelas, T. Charpentier, Mélanie Moskura, Cyrielle Jardin, Alexandre Dauzères

To cite this version:

Fructueux Jesugnon Sohounme, Mejdi Neji, Nicolas Seigneur, Katia Schörle, Arnaud Coutelas, et al.. Hydration mechanisms in Roman seawater concrete: Archaeological analogue for validation of long-term ageing reactive transport model. Cement and Concrete Research, 2026, 201, pp.108114. ⟨10.1016/j.cemconres.2025.108114⟩. ⟨hal-05413775⟩

HAL Id: hal-05413775
https://minesparis-psl.hal.science/hal-05413775v1

Submitted on 20 Mar 2026

Cement and Concrete Research 201 (2026) 108114

Contents lists available at ScienceDirect

Cement and Concrete Research

journal homepage: www.elsevier.com/locate/cemconres

Hydration mechanisms in Roman seawater concrete: Archaeological analogue for validation of long-term ageing reactive transport model

Fructueux Jesugnon Sohounme [a,*], Mejdi Neji [a], Nicolas Seigneur [b], Katia Schörle [c], Arnaud Coutelas [d], T. Charpentier [e], Mélanie Moskura [e], Cyrielle Jardin [f], Alexandre Dauzères [a]

[a] *Autorité de sûreté nucléaire et de radioprotection (ASNR), PSE-ENV/SPDR/LETIS, F-92260, Fontenay-aux-Roses, France*
[b] *Mines Paris PSL, Centre de Géosciences, France*
[c] *Aix Marseille Univ, CNRS, CCJ, Aix-en-Provence, France*
[d] *UMR 8546 CNRS-ENS-EPHE (PSL), France*
[e] *NIMBE, CEA, CNRS, Université Paris-Saclay, CEA Saclay, F-91191, Gif-sur-Yvette cedex, France*
[f] *Autorité de sûreté nucléaire et de radioprotection (ASNR), PSE-ENV/SPDR/LT2S, F-92260, Fontenay-aux-Roses, France*

ARTICLE INFO

Keywords:
Roman hydraulic cement
Pozzolana
Calcium aluminate silicate hydrate
Pozzolanic reaction
Nanoindentation
Reactive transport modeling
HYTEC

ABSTRACT

Cement-based materials are considered for sealing plugs in deep geological disposal of radioactive waste. Ensuring their long-term durability is critical for safety over millennia. The Roman Concrete (RoC) project uses ancient Roman underwater concretes as analogues to validate reactive transport models for long-term ageing. This study focuses on hydration mechanisms in Roman concrete made with Phlegrean pozzolan, slaked lime, and seawater. Various techniques (XRD, SEM-EDS, NMR, nanoindentation, microtomography, ICP-OES, ion chromatography) were used to characterize hydration products. Casting underwater led to aragonite and brucite layers with a 60 GPa Young's modulus, protecting the concrete from further degradation. In the core, pozzolanic reactions produce C-(A)-S-H phases (Ca/Si = 1.2; Al/Si = 0.2) with a modulus of 12 GPa. HYTEC modeling confirmed the mechanism: incongruent pozzolan dissolution releases ions (K^+, SiO_4^{4-}, Al^{3+}, Na^+), promoting C-(A)-S-H formation and portlandite consumption.

1. Introduction

Roman concretes are attracting considerable scientific interest because of their durability, as demonstrated by their preservation despite being in contact with seawater over two millennia. Several studies on roman concretes have been carried out to find the characteristics of the raw materials, the recipe used by the Romans 2000 years ago and the cementation processes of Roman binders [1–6].

The writings of the architect Vitruvius in the second half of the first century BCE, described the cementitious materials used by Romans and how they built underwater concrete [7]. He emphasized the use of a powder (*pulvis*), that we now call pozzolan, which reacts with lime to provide durable strength to the structures in the sea. He pointed out that the material was found in the Phlegrean fields, in the surrounding of Baïa, a town adjacent to Pozzuoli (ancient Puteoli), from whence the modern name derives. Subsequent studies, such as the ROMACONS project [1], have highlighted the use of this pozzolan in Roman harbors across Italy, including Portus, Anzio, Santa Liberata, and Cosa. Beyond Italy, pozzolan from this geographic origin was also employed in the construction of harbors throughout the Mediterranean region. It was proved that pozzolan was transported from the Bay of Naples, more than 2000 km away for the antic harbor of *Caesarea Maritima*, dating from the end of the first century BC [1]. The use of this pozzolan in the harbor of Chersonisos in Crete was proved as well [8,9], and ancient builders probably realized that the pozzolan from the Bay of Pozzuoli was among the most reactive in the Roman Empire [1].

In addition, the ROMACONS project culminated in an experimental archaeological campaign at Brindisi in September 2004, which made a major contribution to our knowledge of how to make Roman-style concrete for marine structure based on Vitruvius instructions [10]. Vitruvius has indicated that the pozzolan/lime ratio was around 2. But the components are not explicitly stated to be measured by volume instead of weight and uncertainties remain regarding the lime nature (quicklime or slaked lime). Oleson et al. [10] assumed that Vitruvius was referring to slaked lime and that components were measured by volume but there is no certainty about the quantity of water. Goldsworthy et al.

---

* Corresponding author.
E-mail address: fructueux-jesugnon.sohounme@asnr.fr (F.J. Sohounme).

https://doi.org/10.1016/j.cemconres.2025.108114
Received 30 September 2025; Received in revised form 26 November 2025; Accepted 5 December 2025

[11] demonstrated using an industrial lime putty that a pozzolan-to-lime putty volume ratio of approximately 3 yields good mechanical properties. In the Brindisi experiment, the authors adjusted the Vitruvian formula to use 2.7 parts pozzolan for 1 part slaked lime in the upper part of the pilar [10,12]. The chemical analyses on sample cored from the Brinsidi reconstructed pila (upper part) after 6 months of curing showed similarity with the chemical composition of the Santa Liberata 2000 years old roman concrete [10,12]. This point confirms the good consistency of the chosen raw materials.

Nowadays, cement-based materials are widely used in the nuclear industry for radioactive waste management [13–18]. They are even considered for plugs to confine the sealing structures (expansive bentonite-based sealing core) in the context of French deep geological disposal of radioactive waste [19]. The concept of deep disposal of long-lived radioactive waste is based on the idea that some geological formations (host rocks) can contain the waste packages deposited in them over very long periods, until the waste returns to a negligible level of hazard potential [20]. It is necessary to assess the performance of repository materials over the long timescales of interest and thus ensure safety. Several studies have been interested in durability of such materials [21–24]. Reactive transport modeling has also been used to understand and quantify the relevant processes occurring during various concrete degradations. These models are validated based on short-term observations, and are then extrapolated to predict the long-term ageing of concrete [25–29]. However, there is no guarantee that model extrapolation over large timescales is valid. Previous study has addressed the subject of the long-term behavior of C-S-H based on Gallo-Roman mortar [30]. But this study did not focus on the validation of long-term ageing reactive transport models nor on multi-ionic attacks in saturated media as will be the case of concrete plugs in the deep geological disposal after the closure by sealing structures. The Roman Concrete (RoC) project initiated by the French Institute for Radiological Protection and Nuclear Safety (IRSN), aims to validate the method of long-term extrapolation of reactive transport simulations. This will be performed through an archaeological analogue approach [31,32] focusing on the ageing of roman underwater concretes. This choice is justified by two main reasons. First Roman seawater concretes are immersed in seawater which has a chemical composition qualitatively equivalent to that of host rock (same chemical species with different concentrations) and therefore in both cases it is multi-ionic attacks in saturated media. Both concretes are subjected to leaching, carbonation, sulfate and magnesium attacks. Secondly, there are reliable archaeological studies such ROMACONS project [1] on materials and process used by Roman two thousand years ago to make their concretes. Thus, the traditional approach of manufacturing, degrading and calibrating a reactive transport model will be done on representative roman concretes.

This paper summarizes the first part of the RoC project. It aims to understand the hydration mechanisms of underwater roman concrete using raw materials as close as possible to those used by Romans 2000 years ago. So, mortar was made up with pozzolan from Phlegrean fields, slaked lime and seawater as proposed by Vitruvius. Different experimental techniques (XRD, SEM-EDS, NMR, nanoindentation, and X-ray microtomography) were used to study the evolution of the mineralogical, chemical and micromechanical properties of the solid phase during hydration. On the other hand, ICP-OES, ionic chromatography and pH measurement were used to study the pore water solution evolution during hydration. The interpretation of experimental results was supported by reactive transport modeling with HYTEC [33]. A calibrated reactive transport model based on experimental results was developed to simulate the hydration mechanism in roman underwater concretes. Extrapolation of this model was compared with chemical and mineralogical characterizations of the Brindisi pila (19 years ageing). This study uniquely combines in situ samples, laboratory cast samples, and modeling to investigate not only the hydration mechanisms but also the spatial and temporal differences across the interfaces and depths of the samples.

2. Materials & methods

2.1. Materials

In September 2023, a core of 9 cm of diameter and 78 cm length was extracted from Brindisi Pila. The core was drilled on the north face at 80 cm from the seawater level (Fig. 1b). The casting protocol can be found in the work of Oleson et al. [10]. This core will be identified as B19 (Brindisi 19-year-old sample) in this work.

Natural pozzolan was obtained from the Flegrea quarry in the Phlegrean region. The industrial slaked lime putty CL90S commercially available from Saint Astier was used in this study for replicating Roman mortar [10]. Natural seawater was extracted from the English Channel off the coast of Cabourg (France). Its composition is compared to that of the Mediterranean Sea in Table 1, showing no significant changes. Note that English Channel seawater was used to make RHUM (Roman Hydrated Underwater (seawater) Mortar) sample for microtomography. For logistical reasons, other tests samples were made with Mediterranean seawater.

The chemical composition of the pozzolan is reported in Table 2 and the component characteristics of the lime putty are reported in Table 3. The pozzolan was sieved with a 500 μm sieve before use to remove large grains. The use of a 500 μm sieve is simply a choice, on the one hand to have a representative elementary volume compatible with characterization techniques, while optimizing sieving time, and on the other hand to ensure the repeatability of the tests. No aggregate, as tuff, was included in the formulation to focus on the binding matrix behavior. To increase the workability of the fresh cement paste, a certain amount of seawater was added, as done in the ROMACONS project [10].

The recipe used in our study is based on the ROMACONS project and is given in Table 3. The total water to solid mass ratio (w/s) is equal to 0.53, the calcium to silica atomic ratio (Ca/Si) is 0.64 and the aluminum to silicon atomic ratio (Al/Si) is equal to 0.36 ($Al_2O_3/SiO_2 = 0.18$). The bulk densities of pozzolan and lime putty were calculated by dividing the masses by the corresponding bulk volumes. The bulk densities of pozzolan and lime putty are 660 kg/m^3 and 1200 kg/m^3 respectively. Two kinds of samples have been made with this recipe.

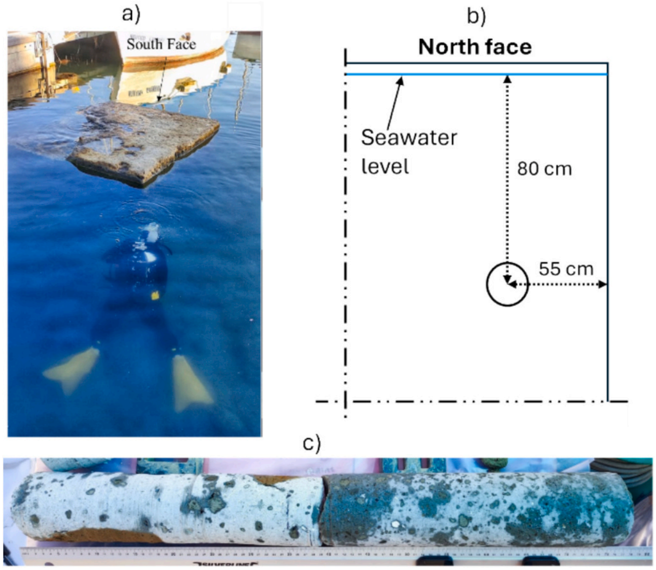

Fig. 1. (a) Drilling core from the Brindisi pila (b) Drilling localization (c) drilled core sample. The differences in visual appearance between the two parts of the extracted core are related to different drying levels, as the left part was extracted before the right one.

Table 1
Composition of compounds in seawater extracted from the English Channel off the coast of Cabourg (France) and the Mediterranean Sea, showing that their chemical compositions are relatively close.

Compound	Mg^{2+}	Ca^{2+}	Na^{+}	K^{+}	Cl^{-}	SO_4^{2-}	HCO_3^{-}	pH	Reference
Mediterranean Sea [mg/L]	1600	450	11,400	397	22,330	3070	–	–	[34]
English Channel sea [mg/L] /pH	1195	417	9611	427	17,834	2519	146	8.2	This study

Table 2
Chemical composition and Loss on ignition (L.O.I) of pozzolan from the Flegrea quarry determined by ICP-OES.

Oxides	Al_2O_3	CaO	Fe_2O_3	K_2O	MgO	MnO	Na_2O	P_2O_5	SiO_2	TiO_2	L.O.I
Mass (wt %)	15.87 ± 1.06	2.52 ± 0.14	3.18 ± 0.22	7.21 ± 0.53	0.80 ± 0.05	0.11 ± 0.05	3.25± 0.21	0.14 ± 0.01	51.96 ± 4.25	0.38 ± 0.03	11.23 ± 0.09

Table 3
Composition of compounds of replicated roman mortar.

Compounds			Mass ratio	Volume ratio
Lime putty (data from producer)	Mineral composition (g/100 g of lime putty)		0.44	0.31
	Portlandite	35.5		
	Calcite	4.5		
	Pure water	60		
Pozzolan (from Flegrea quarry in Phlegrean fields)			0.48	0.62
Sea water			0.08	0.07

- After casting, some samples were embedded in sealed bag for curing at atmospheric temperature (20 °C), these samples are named SBM (sealed bag mortar).
- The other samples are submerged with one face directly in seawater with partial pressure of CO_2 at 400 ppm (partial pressure of ambient CO_2), the other faces of the samples are waterproof to ensure a unidirectional diffusion. These kinds of samples are named RHUM (roman hydrated underwater (seawater) mortar).

The SBM samples were used to study the hydration processes in roman underwater sound zone and RHUM samples were used to focus on the mortar-seawater interface during hydration of Roman underwater concrete. This experiment aims to replicate and study on a laboratory scale the processes that took place at the mortar-seawater interface of roman underwater mortar. Note that the use of lime putty added some amount of pure water in the system (Table 3).

2.2. Methods

2.2.1. Solid phase analysis

Loss on ignition (L.O·I) test was carried out on the pozzolan in accordance with standard NF P18–807. Two crucibles containing 1 g of pozzolan were subjected to 450 °C in a muffle furnace Thermo Scientific™ for 2 h. Then crucibles were removed from the furnace and placed in desiccators for cooling at room temperature. The LOI value is the percentage of mass lost during ignition of the sample.

ICP-OES analysis was performed to determine the pozzolan's chemical composition as done by [35] on pulverized cement binder. A quantity of 150 mg of pozzolan was fused with 900 mg of lithium metaborate at 550 °C for 5 min for the first heating stage and at 980 °C with stirring speeds and angles that vary over time for 15 min for the second heating stage. The fusion residue was dissolved with 179 mL of HNO_3 of 1 mol/L, 20 mL of H_2O_2 (10 % by volume) and 1 mL of Glycerol (0.5 % by volume). The solution was diluted for the determination of Al, Ca, Fe, K, Mg, Mn, Na, P, Si and Ti expressed as Al_2O_3, CaO, Fe_2O_3, K_2O, MgO, MnO, Na_2O, P_2O_5, SiO_2 and TiO_2 (Table 2). The characteristics of used ICP-OES are provided in the following section (Pore solution analysis).

SEM-EDS analyses were carried out on carbon metallized polished sections. The acquisition was performed on SEM Zeiss EVO-25 with two EDS Brüker 7030 XFlash at 15 keV. The pixel size is 2.8 μm, at the limit of the interaction pair for this type of material [36]. Since the images obtained contain 401,240 pixels, the average number of photons per pixel exceed 4000 to estimate the intensity distribution and 10,000 to enable atomic quantification. A Phi-Rho-Z quantification method [37] was applied on hyperspectral images to extract in each pixel the atomic distribution. A clustering method based on the Gaussian Mixture Model [38–40] was applied to the quantification results (Fig. 5) or the intensity distribution (Fig. 9) to group pixels according to their chemical signature. The number of clusters was determined using the elbow method [41,42]. Secondary electron (SE) images were acquired using a FEG-SEM Thermofisher QUATTRO S operated at an accelerating voltage of 3 kV. Prior to analysis, the samples were coated with a layer of gold (Au).

The XRD analyses presented in this paper were carried out with an Aeris Research Edition diffractometer from Malvern-Panalytical in $\theta - 2\theta$ configuration, under CuKα radiation ($\lambda = 1.54$ Å) with a divergence slot of 0.5° and a rotation platform. The scan region was in the range (2θ) from 5° to 70°. The analyses were performed on slices of polished samples during 20 min for RHUM samples. The distance between the surface and each polished slice was approximated with a digital instrument as done by Dewitte et al. [43]. The analyses were performed on crushed samples during 2 h for SBM. The Quantitative Phase Analysis (QPA) was performed with Panalytical HighScore Plus [44] according to the recommendation of Scrivener et al. [45]. The contribution of C-A-S-H and the amorphous part of the pozzolan were estimated using the PONCKS approach [46,47]. In fact, a diffraction pattern of a 5-year-hydrated C-S-H with Ca/Si ratio of 1.2 was used to fit the main component C-(A)-S-H. The PONCKS approach was validated using thermogravimetric analysis (TGA) as recommended by Li and Scrivener [46]. To maintain conciseness, TGA results are not presented in this paper. The excellent mineralogical literature on Roman mortars [2,4,48–51] was considered for the choice of minerals in the XRD database. The minerals identified in this paper were extracted from Crystallography Open Database (COD) as detailed in Table 4.

Nanoindentation tests were performed using a nano-indenter (NHT^3,

Table 4
References of crystallographic data used for Rietveld analysis.

Mineral	COD reference code	Reference
Calcite	2,100,993	[52]
Ettringite	9,015,084	[53]
Portlandite	9,000,113	[54]
Phillipsite-Ca	9,011,149	[55]
Hydrocalumite	9,009,353	[56]
Analcime	9,002,000	[57]
Biotite	9,001,264	[58]
Sanidine	9,009,662	[59]

Anton Paar ®) with a Berkovich tip on polished sections (prepared for SEM-EDS analysis) of the SBM, RHUM and B19 samples. The tests were controlled for depth and force (Max depth = 300 nm, loading rate = 12 mN/min, pause = 10 s) on a grid domain of 350 μm * 350 μm (distance between indent = 10 μm) as done by [60].

^{29}Si and ^{27}Al MAS NMR were performed on the Flegrea quarry pozzolan and SBM samples of different hydration times using a Bruker Avance IV NEO 500WB spectrometer (11.7 T magnetic field) for the ^{27}Al nucleus and a Bruker Avance II 300WB spectrometer (7 T magnetic field) ^{29}Si nucleus. Spectra were acquired with a Bruker CPMAS (Cross-Polarization Magic Angle Spinning) 4 mm probe (powder samples compacted in ZrO_2 rotors, about 100 mg) at a spinning frequency of 12.5 kHz (rotation period 80 μs).

X-ray microtomography analyses were performed on RHUM samples after 0.25, 0.7, 2, 4, 6 and 8 months in seawater. A Bruker SkyScan 1173 CT scanner was used, equipped with a 2 k pixel detector working at 130 keV and 61 μm. Acquisitions were performed with a 180° rotation at step of 0.2°, frame average numbers of 8, voxel size of 11.8 μm. A median filter of radius 2 was applied after data reconstruction. To segment calcium carbonate phases from μCT data, including surface crusts, four representative slices per scan were manually labeled using a Gaussian Mixture Model (GMM) [40], producing binary masks (calcium carbonate phases vs. other phases). These were used to train a U-Net CNN [61] with dilated convolutions and global context injection. The model was optimized using the Adam optimizer and a binary focal cross-entropy loss to address class imbalance. Training employed early stopping and learning rate reduction. Segmentation was then applied to sub-volumes composed of stacked 2D slices (40,000 voxels each), enabling 3D reconstruction of surface crusts over time. [62]

2.2.2. *Pore solution analysis*

The chemical composition and pH of the pore solution were determined at different periods of hydration. The pore solution was obtained using an ex-situ leaching method [63]. For each period of hydration, 6 g of a hardened SBM sample were ground and put in suspension with 54 mL of Milli-Q water in glove box kept under nitrogen atmosphere. These amounts were used to have a water to solid ratio of 9 mL/g as done by Codina [64]. The suspension was stirred for 24 h and was filtered through 0.45 μm PES VWR® filters. Some amount was acidified to 2 % of nitric acid to prevent any solid phase precipitation until inductive coupled plasma optical emission spectroscopy (ICP-OES, Thermo Fisher ICAP™ 7600 Duo) analysis. For this test, solutions were diluted at dilution factor of 1×, 10×, 100×, 1000× and 10,000× depending on the element concentration as the maximum that can be detected in our analysis condition is 5 mg/L. The concentration of Cl and sulfate ions were measured on solution without acidification using ionic chromatography (930 Compact IC Flex from Metrohm). The pH measurements were performed immediately after filtration in the glove box with a pH meter Multi 3420 WTW. The pH electrode was calibrated against potassium dihydrogen phosphate/dihydrogen sodium phosphate solutions of known concentrations.

2.2.3. *Reactive transport modeling*

2.2.3.1. Reactive transport equations. Modeling of the hydration and evolution of SBM and RHUM samples was performed using the reactive transport code HYTEC [33], which has been used extensively in the context of cementitious materials [65–68]. HYTEC accounts for the multi-species transport coupled to the various geochemical reactions (aqueous complexation, redox reactions, sorption, mineral dissolution/precipitation, …). The coupling between chemistry and diffusive transport was simulated using (Eq. (1)), in water-saturated conditions [33]. D_e is the effective diffusion coefficient [m^2/s] for all the dissolved species, $\varnothing$ is the material total porosity, c_i and $\overline{c_i}$ are respectively the basis species i mobile total concentration [mol/L] in solution and immobile total concentration [mol/L].

$$\frac{\partial \varnothing c_i}{\partial t} = \nabla.(D_e(\varnothing)\nabla c_i) - \frac{\partial \varnothing \overline{c_i}}{\partial t} \tag{1}$$

The porosity change induced by mineral dissolution and precipitation impacts the transport properties [69]. This modification is considered here using a modified version of Archie's law [33]:

$$D_e(\varnothing) = D_e(\varnothing_0)\left(\frac{\varnothing - \varnothing_c}{\varnothing_0 - \varnothing_c}\right)^{\alpha} \tag{2}$$

where α is an empirical coefficient usually equal to 3 for cementitious materials [66], $\varnothing_0$ is the initial porosity equal to 0.5, and $\varnothing_c$ is a threshold under which diffusion stops and is equal to 0.02.

2.2.3.2. Chemical and physical data. The 2020 version of Thermoddem thermodynamic database was used [70]. The properties of all phases considered during the modeling are given in Table 5. In addition, due to the limited amount of C-A-S-H phases in this database, the 5CA C-A-S-H description of CEMDATA was added [71].

2.2.3.3. Modeling approach. The initial mineralogy was set according to the results obtained by QPA XRD (based on Rietveld + PONKCS) and presented in Fig. 4. All the solid phases are modelled according to the thermodynamic equilibrium. In addition, a kinetic approach is used to describe the pozzolan reactivity. The pozzolan dissolution is modelled as incongruent with two solid phases: “P” and amorphous silica. The “P” is a created phase with the following reaction:

$$P + H^{+} \rightarrow 0.2\,Al^{3+} + 0.15K^{+} + 0.25Na^{+} + H_4SiO_4 \quad with\ logK = 3 \tag{3}$$

which was derived from an aggregate composition of Sanidine and Analcime. This phase dissolution intends to drive the releasing of Al^{3+}, K^{+}, and Na^{+} to fit experimental data obtained from the pozzolan dissolution by ICP-OES. Thus the “P” reactivity was adjusted to represent porewater composition evolution during the hydration mechanism, following the kinetic rate law:

$$R = \frac{d[P]}{dt} = kS_s[P]\left(\frac{Q}{K} - 1\right) \tag{4}$$

with k being the rate coefficient (2 × 10^{-11} mol/m^2/s) with a specific surface area S_s of 1 m^2/g. Q represents the ion activity product and K the solubility constant from the database. Precipitation of this phase is not allowed in the model to follow experimental observation. The other source of silica, represented by the presence of amorphous silica (Fig. 3), has a rate constant of 2 × 10^{-11} mol/m^2/s and a specific surface area of 30 m^2/g. Note that the choice of kinetic expressions and parameters have been motivated to reproduce as simply as possible the observed early trends during the hydration processes. Our focus is on the precipitation of hydrates and the mineralogical evolution over time. Then the early transformation of Phillipsite to analcime reported by Jackson et al. [5] was not considered here to focus on pozzolanic and post-pozzolanic reactions.

Two simulations are performed. First, batch simulations are performed to understand the hydration processes and their effects on porewater composition and mineralogy. This simulation includes the various potential hydrates (Ettringite, Gypsum, Friedel Salt, C-(A)-S-H of varying Ca/Si ratio, …), which are listed in Table 5. Strätlingite, calcium aluminate hydrate and Hc(carbon aluminate phases) predicted by previous study [72] are not considered here as XRD did not show their presence. Secondly, a 1D reactive transport simulation is performed to study how the interface with seawater affects the equilibrium reaction. The 1D configuration is justified for the RHUM sample since only the top wall of the mortar is in contact with seawater. The domain considered for the modeling is made up of three rectangular sub-domains. The first one represents the seawater tank, the second is for the mortar-seawater

Table 5
Thermodynamic formation constants at chemical equilibrium of the solid phases considered in geochemical modeling, [70] cited by [65]. (1) 5CA C-A-S-H description of CEMDATA [71]. (2) The logK (25 °C) of Friedel salt has been increased from −74.946 to −72.946 to favor its precipitation in line with hydrocalumite precipitation (Fig. 4).

Solid phase	Chemical equation	Log K 25° C	Density (kg/m3)
Cement hydrates			
C1.6SH	$3.2Ca^{2+} + 2\ H_4SiO_4 + 2.6128\ H_2O - 6.4H^+ \rightarrow (CaO)_{3.2}(SiO_2)_2(H_2O)_{3.4128}$	−55.99	2506
C1.4SH	$2.8Ca^{2+} + 2\ H_4SiO_4 + 1.9144\ H_2O - 5.6H^+ \rightarrow (CaO)_{2.8}(SiO_2)_2(H_2O)_{3.1144}$	−46.93	2447
C1.2SH	$2.4Ca^{2+} + 2\ H_4SiO_4 + 1.1895\ H_2O - 4.8H^+ \rightarrow (CaO)_{2.4}(SiO_2)_2(H_2O)_{2.7895}$	−38.09	2389
C1SH	$2Ca^{2+} + 2\ H_4SiO_4 + 0.3978\ H_2O - 4H^+ \rightarrow (CaO)_2(SiO_2)_2(H_2O)_{2.3978}$	−29.47	2358
C0.8SH	$1.6\ Ca^{2+} + 2H_4SiO_4 – 0.218\ H_2O - 3.2\ H^+ \rightarrow (CaO)_{1.6}(SiO2)_2(H_2O)_{2.182}$	−21.18	2299
5CA$^{(1)}$: C1.25A0.125SH1.625	$1.25Ca^{+2} + 0.25Al^{3+} + H_4SiO_4 + 1.25H_2O -3.25H^+ \rightarrow (CaO)_{1.25}(SiO_2)(Al_2O_3)_{0.125}(H_2O)_{1.625}$	−21.62	3017
Ettringite	$2Al^{3+} + 6Ca^{2+} + 3SO4^{2-} + 38\ H2O \rightarrow Ca_6Al_2(SO_4)_3(OH)_{12}\cdot(H_2O)_{26}(H+)_{12}$	−57.00	1767
Portlandite	$Ca^{2+} + 2H_2O \rightarrow Ca(OH)_2 + 2\ H^+$	−22.81	2241
Other phases			
Gypsum	$Ca^{2+} + SO_4^{2-} + 2\ H_2O \rightarrow CaSO_{4.0}.2\ H_2O$	4.61	2305
Calcite	$Ca^{2+} + HCO_3^- \rightarrow CaCO_3 + H^+$	−1.85	2710
Gibbsite	$Al^{3+} + 3H_2O \rightarrow Al(OH)_3 + 3\ H^+$	−7.73	2441
Amorphous silica	$SiO_2(aq) \rightarrow SiO_2(am)$	2.69	2072
Friedel Salt	$2\ Al^{3+} + 4Ca^{2+} + 2Cl^- + 16\ H_2O \rightarrow Ca_2Al(OH)_6(Cl,\ OH)\cdot 2\ H_2O + 12H^+$	−74.946 −72.946$^{(2)}$	2032

interface. The last is the RHUM sample. The seawater tank volume is 5×10^{-4} m^3 and modelled as one rectangular grid of 40 μm in width, the same grid was used for the second zone. The RHUM sample volume is 2.1×10^{-5} m^3 and modelled as a rectangular grid of 0.5 mm in width composed of 125 rectangular meshes. The seawater porosity was adapted to respect the experimental ratio between the volume of seawater and the RHUM sample volume (Seawater/RHUM = 24). Seawater chemistry is in equilibrium with calcite and a constant atmospheric p(CO2) = 400 ppm. Total dissolved concentrations of major elements are reported in Table 1 consistent with mediterranean seawater composition.

The initial effective diffusion coefficient D_e was 2×10^{-9} m^2/s in the water. The initial effective diffusion coefficient D_e of the mortar was 1×10^{-9} m^2/s. This value is higher than that of a hardened cement paste [73], because in the initial state the RHUM sample had not hardened.

A schematic representation of the overall approach, including the multi-technique characterization performed, is shown in Fig. 2.

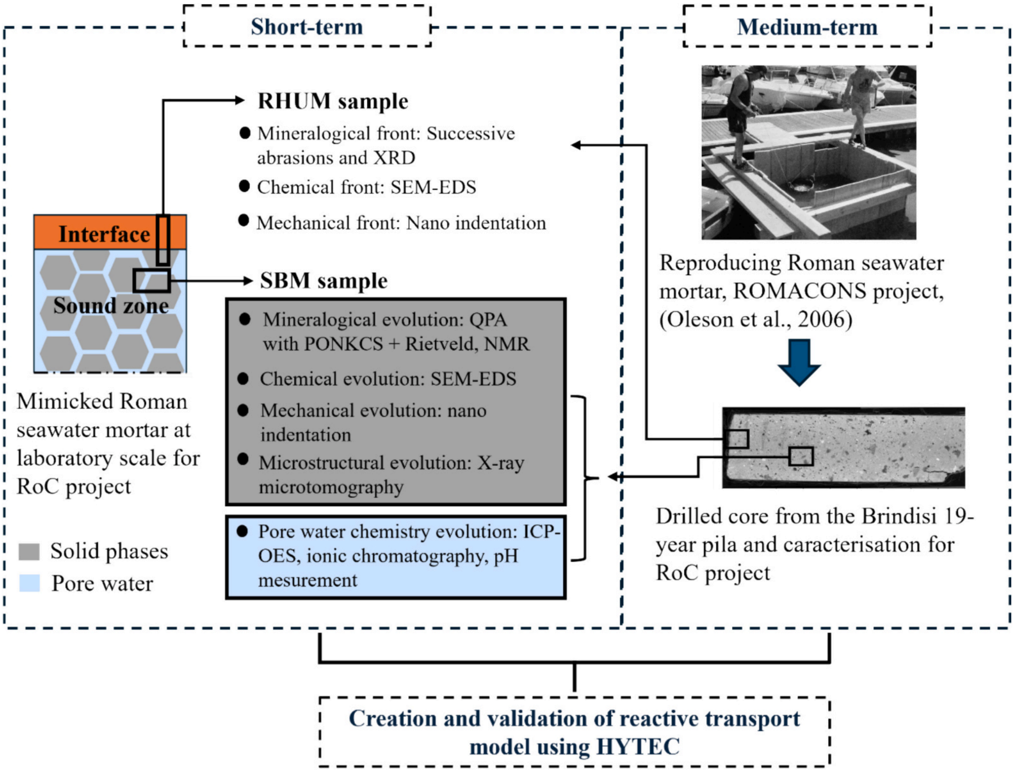

Fig. 2. Schematic representation of the overall approach, including the multi-technique characterization per-formed.

3. Results

All raw data and post-processing scripts used for this study can be found at:

https://www.data.gouv.fr/fr/datasets/data-of-article-hydration-mechanisms-in-roman-seawater-concrete/.

3.1. Hydration processes on the internal domain of cast samples referred as sound zone

3.1.1. Mineralogical evolution during hydration

The QPA XRD analyses were performed on the Flegrea quarry pozzolan to determine its mineralogical distribution. Results are presented in Fig. 3 (a).

The XRD pattern shows a significant hump with minor peaks. This hump is related to the amorphous phases [74]. It means that the Flegrea quarry pozzolan is mainly amorphous with minor crystallized minerals. The amorphous phase is the volcanic glass phase of the pozzolan and is estimated to represent 90 wt-% of the pozzolan with some crystalline minerals such as sanidine (7 wt-%), analcime (2 wt-%) and phillipsite-Ca (1 wt-%). Note that sanidine, analcime and phillipsite were also found in Yellow Napolitan Tuff used for the experimental reproduction of the Roman concrete at Brindisi [1]. The hump was extracted from the XRD pattern of the pozzolan, representing the amorphous part (the volcanic glass phase). The fitted crystallographic information was then used to quantify the amount of amorphous phase of pozzolan in B19 and SBM at different periods of hydration.

Quantitative phases analyses (QPA) based on Rietveld + PONKCS methods were performed on B19 and are presented in Fig. 3 (b). The main phases are C-(A)-S-H type phase (57 wt-%), unreacted amorphous phase of the pozzolan (AP) (20 wt-%) and hydrocalumite (10 wt-%). No traces of Portlandite were noticed in the matrix. However previous studied conducted by the ROMACONS team on the same pila [49,50] showed the presence of portlandite until sixty months. The portlandite

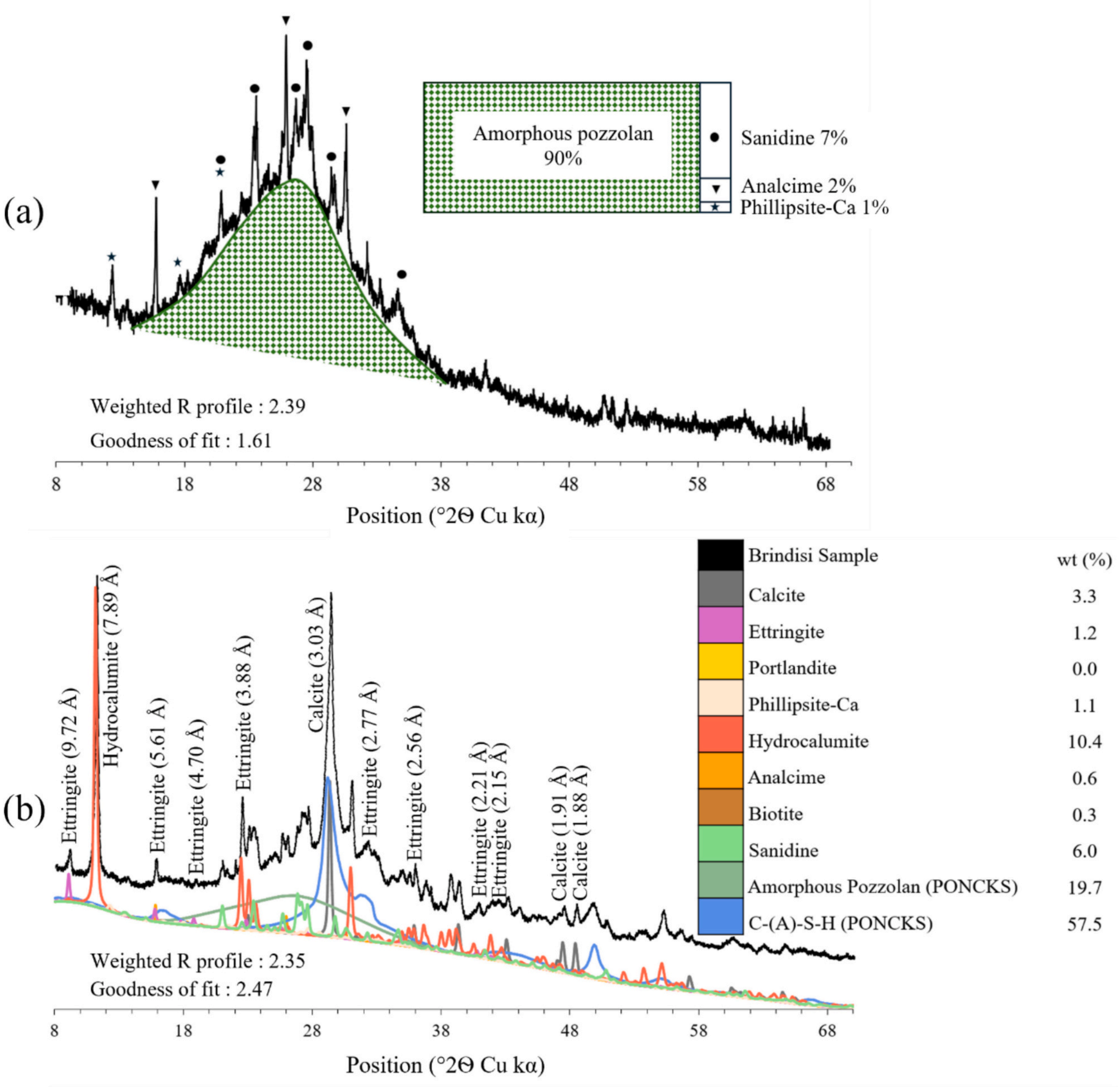

Fig. 3. (a) QPA XRD of pozzolan from the Flegrea quarry showing that it is mainly amorphous with minor minerals. (b) Pattern decomposition of B19. Note that amorphous pozzolan stands for the amorphous phase of the pozzolan which is the volcanic glass phase of the pozzolan.

was completely consumed later. This information can help with the study of reaction kinetics of Vitruvian pozzolanic mortar. A limited amount of carbonation products were detected. This technique (QPA) was also performed on SBM samples for different curing periods. X-ray diffraction data and the post-treated results are available (see Data Availability section). These results are plotted in Fig. 4. It showed that while the amount of amorphous pozzolan (AP) and portlandite (CH) decreased, the amount of C-(A)-S-H phase increased, confirming the pozzolanic reactions to form C-(A)-S-H. At 172 days of curing the amount of CH (about 5 wt%) agrees with that determined by TG on B19 at 6 months of curing (6.2 wt% at the bottom core) [12]. The amount of hydrocalumite increased as well. The secondary phases showed on Fig. 3 (b) did not exhibit significant variations during hydration and were not included in Fig. 4 for clarity reasons.

^{29}Si and ^{27}Al MAS NMR were performed on the Flegrea quarry pozzolan and SBM samples of different hydration times to evaluate Al and Si coordination states during the hydration of "Roman" mortar. ^{29}Si MAS NMR investigation (Fig. 4b) shows significant contributions in two main ranges −100 to −90 ppm and − 90 to −77 ppm. The first one is a wide band with a chemical shift around −97 ppm corresponding to a Q^3 environment consistent with a phyllosilicate structure with infinite sheets [75], suggesting that Flegrea pozzolan contains such structural motifs. In SBM samples, the intensity of this −97 ppm signal progressively decreases with hydration, indicating pozzolan consumption, in line with XRD results (Fig. 4a). The contributions in the ranges −90 to −77 ppm show chemical shifts which are related respectively to branching positions Q^2 and Q^1 of C-(A)-S-H of previous study [76]. Note that these signals are absent or barely detectable in the pozzolan and increase over time in SBM samples, reflecting the growth of the C-A-S-H phase, as also evidenced in Fig. 4. ^{27}Al MAS NMR spectra show comparable trends. Initially, aluminum in the pozzolan is mainly present as a tetrahedrally coordinated species around 55 ppm, which decreases with hydration. Hydration influences two additional spectral regions. First, a signal in the 70–80 ppm range, initially absent or barely visible, emerges and intensifies in SBM samples, corresponding to tetrahedrally coordinated Al (Al$_{IV}$) in C-A-S-H [77]. Second, a region between 10 and 20 ppm reflects octahedrally coordinated Al [76]. A resonance at ~9.2 ppm attributed to Friedel's salt is also observed [77–79], and its increasing intensity with hydration confirms the formation of hydrocalumite-like phases, as supported by the XRD analysis (Fig. 3a). [76] [77–79].

3.1.2. *Pore water chemistry evolution during hydration*

The evolution of the pore water pH and composition was measured. Results from B19 and SBM sample after 1, 7, 40, 119 and 283 days of hydration are presented in Fig. 10. The pH seems relatively constant around 12.6 during 283 days. However, the Ca^{2+} decreases with hydration time (from 18 mmol/l after 1 day of hydration to 9 mmol/l after 283 days). The decreasing of calcium with hydration time here is in line with increasing of alkali concentration (K$^+$ and Na$^+$) due to the pozzolan dissolution.

On the other hand, the porous solution pH of B19 is around 12.2 and its calcium concentration is around 2.8 mmol/l. These values are lower than those of SBM. The lower pH is in line with the absence of portlandite in B19 matrix as shown in previous section with XRD analysis.

3.1.3. *Coupling mineralogical and mechanical evolution during hydration*

SEM-EDS analysis was performed on B19 and results from phase recognition were presented on Fig. 5a. Seven main phases were found and the chemical compositions of each are presented in Table 6. Based on these chemical compositions and B19 mineralogical composition estimated by XRD (Fig. 3b), minerals were assigned to each phase (Table 6). Accordingly, the predominant phase (label_0) is $C_{1.2}A_{0.1}SH$. The pozzolan is assigned to the phase of label_1. As EDS measurement depth is 3 μm in our test conditions some mix of minerals is possible.

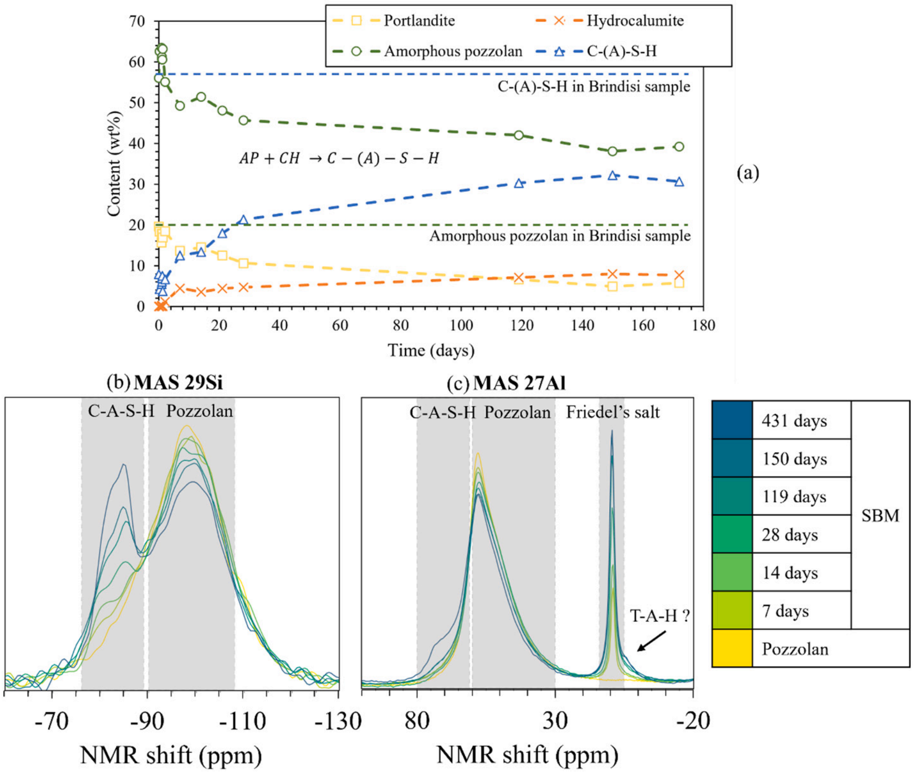

Fig. 4. a) Mineralogical evolution of the main phases of the SBM sample depending on the hydration time showing the decreasing of amorphous pozzolan (AP) and Portlandite (CH) while C-A-S-H and hydrocalumite increased. For clarity reasons the secondary phases are not plotted. Note that amorphous pozzolan stands for the amorphous phase of the pozzolan which is the volcanic glass phase of the pozzolan. b) ^{29}Si and c) ^{27}Al MAS NMR spectra of the Flegrea quarry pozzolan and SBM samples for different hydration times, T-A-H stands for third aluminate hydrate.

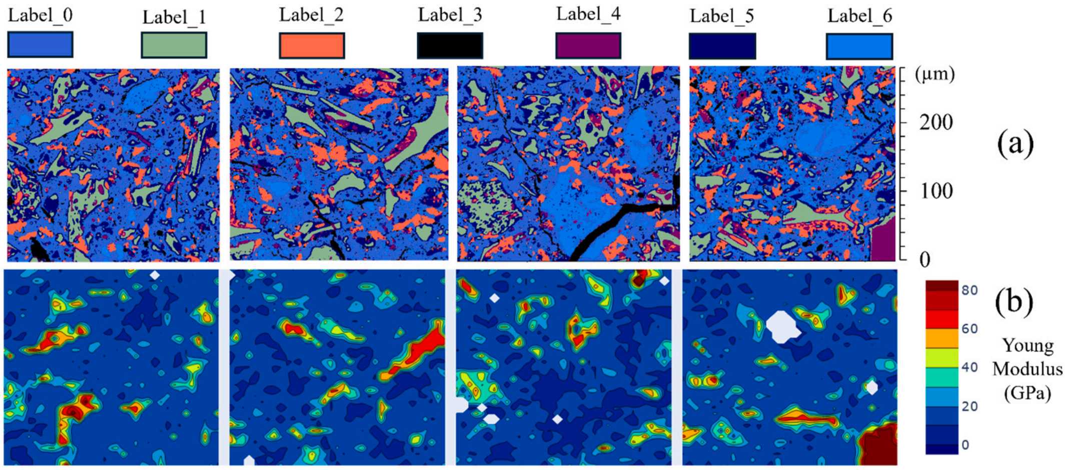

Fig. 5. Chemical and micro mechanical properties of B19: (a) EDS phase recognition showing seven main clusters (estimated with GMM segmentation). Their chemical compositions are summarized in Table 6. (b) Mapping of Young's modulus in B19 sample.

Table 6
Chemical compositions given in atomic percent associated with EDS phase recognition (Fig. 5b) with assigned phases.

Label	0	1	2	3	4	5	6
Ca %	41	5	47	33	28	29	42
Si %	34	55	20	24	35	38	31
Al %	7	18	17	7	17	11	7
Na %	9	7	6	10	8	10	10
Cl %	4	1	7	17	3	1	3
K %	3	12	2	3	5	7	4
Fe %	1	2	1	2	2	2	–
Mg %	1	1	–	1	2	1	–
Ca/Si	1.21	0.09	2.35	1.38	0.80	0.76	1.35
Al/Si	0.21	0.33	0.85	0.29	0.49	0.29	0.23
Potential phase	C1.2A0.1SH	Pozzolan	~ 59 % Hydrocalumite + ~ 41 % C-A-S-H	C-A-S-H + minor Hydrocalumite	?	Pozzolan + Hydrocalumite + C-A-S-H	C1.35A0.12SH

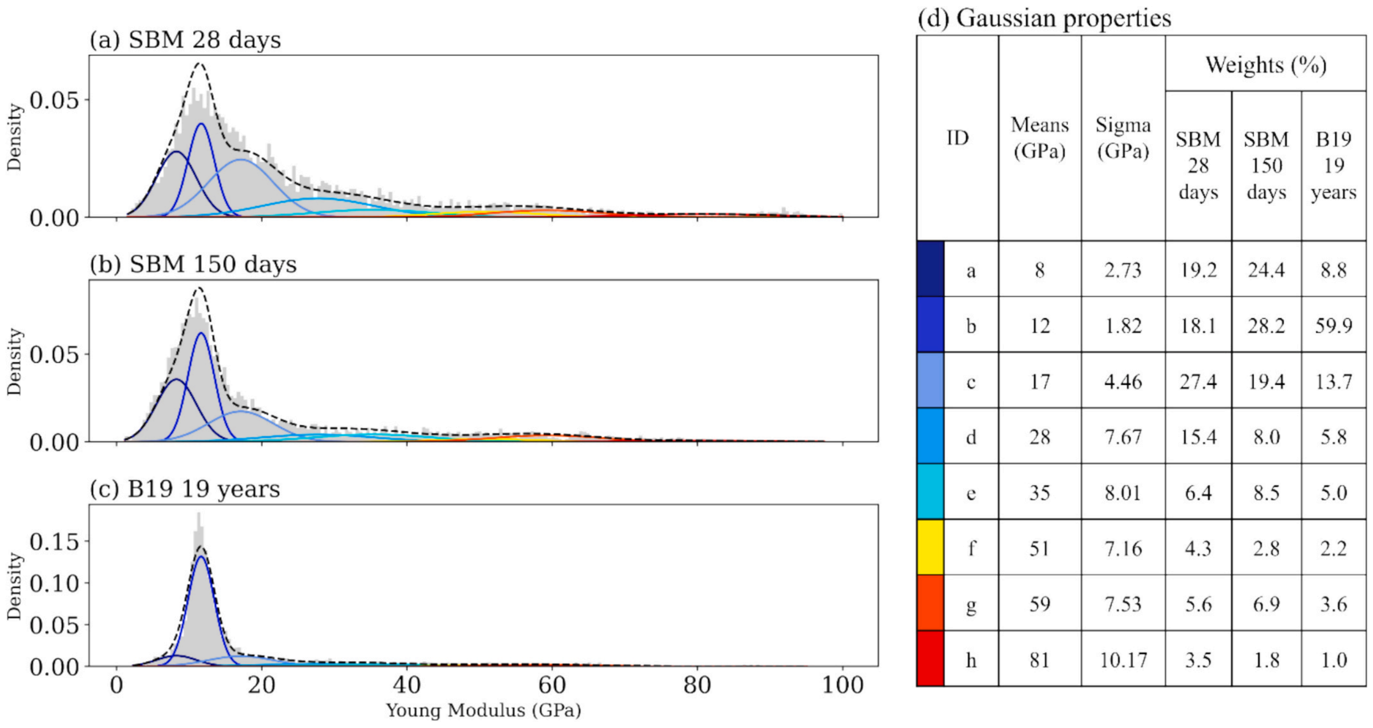

ID	Means (GPa)	Sigma (GPa)	Weights (%) SBM 28 days	Weights (%) SBM 150 days	Weights (%) B19 19 years
a	8	2.73	19.2	24.4	8.8
b	12	1.82	18.1	28.2	59.9
c	17	4.46	27.4	19.4	13.7
d	28	7.67	15.4	8.0	5.8
e	35	8.01	6.4	8.5	5.0
f	51	7.16	4.3	2.8	2.2
g	59	7.53	5.6	6.9	3.6
h	81	10.17	3.5	1.8	1.0

Fig. 6. Nano-indentation results of SBM at: (a) 28 days of hydration, (b) 150 days of hydration and (c) B19 sample. d) Legend and Gaussian properties.

Indeed, phase of label_2 is a mix of hydrocalumite and $C_{1.2}A_{0.1}SH$.

Nanoindentation measurement was performed on SBM samples at 28 and 150 days of hydration time and frequency plots obtained from results are compared with that of B19 (Fig. 6). Note that the four indented zones of B19 sample were the ones analysed by SEM-EDS. Young's modulus mappings in B19 sample are presented with SEM-EDS mapping (Fig. 5b). For all samples a GMM segmentation were used to make phase deconvolution basing on histograms. Eight main clusters (groups) were considered. The Young's modulus values of these groups are centered at a mean of 8, 12, 17, 28, 35, 51, 59 and 81 GPa.

It can be observed that the percentage of cluster of ID_b (12 GPa Young's modulus) increases with hydration time (around 18 %, 28 % and 60 % respectively at 28 and 150 days of hydration and on the Brindisi 19-year-old sample). Note that XRD-QPA (Rietveld + PONKCS) result presented on Fig. 4 showed increasing with hydration time of C-(A)-S-H phase (around 21 wt%, 32 wt% and 57 wt% respectively at 28 and 150 days of hydration and on the Brindisi 19-year-old sample). This mineralogical evolution could be related to the micro mechanical evolution of cluster of ID_b (12 GPa Young's modulus). Then the Young's modulus of C-(A)-S-H phase of roman underwater concrete studied here is about 12 GPa. This value is lower than that estimated by previous studies [80], which reported values ranging from 18 to 36 GPa for C–S–H in cement pastes cured at temperatures close to room temperature. Considering the properties of the C-S-H which gives a Young's modulus greater than 30 GPa [81], its decrease suggests an increase of the porosity, in view of the various studies on the subject. The clusters of ID_c (17 GPa), ID_d (28 GPa) and ID_f (51 GPa) decrease with hydration time. These cluster evolutions could be related to the pozzolan evolution during hydration.

3.2. Hydration processes at the seawater interface

3.2.1. Mineralogical evolution from the mortar-seawater interface (surface) to the internal domain (sound zone) of cast samples

A focus is made here on the processes that occur on the mortar-seawater interface. XRD were performed on a polished slice from the RHUM sample from the interface to the sound zone after 63 days. The diffractograms are presented in Fig. 7. It shows a monocrystal layer (less than 90 μm) of aragonite on the interface. This layer is followed by a polycrystal (from 90 μm to 370 μm) layer composed mainly of brucite and minor minerals such as halite and aragonite. Halite precipitation is induced during the drying associated to the XRD testing. Further down, there is an area (from 430 μm to 720 μm) with brucite, ettringite and hydrocalumite. There is less or no brucite and ettringite starting from 930 μm and 4590 μm respectively. The sound zone, in which Portlandite

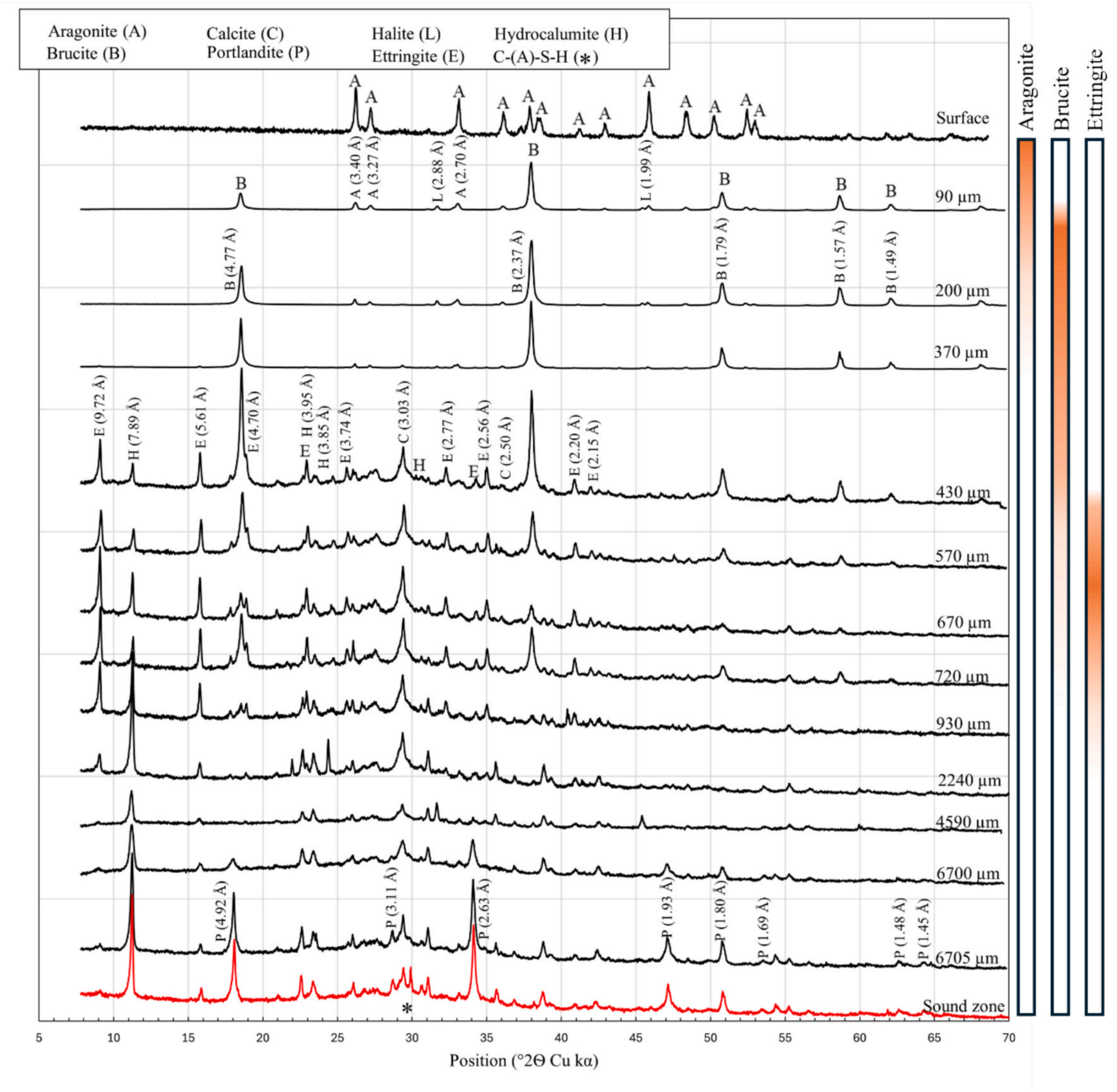

Fig. 7. X-Ray diffraction patterns from the mortar-seawater interface (surface) to the sound zone. XRD tests were performed on the slice of polished RHUM sample after 63 days. Colormaps on the right indicate the precipitation extent of aragonite, brucite and ettringite.

appears, appears at 6700 μm.

X-ray microtomography analyses were performed on the RHUM sample after 0.25, 0.7, 2, 4, 6 and 8 months in seawater and the results are presented in Fig. 8. Segmented data of the crust (Fig. 8a) show its growth with time. The different zones from the mortar-seawater interface to the internal domain (sound zone) are presented in Fig. 8b. A low-density zone can be seen just beyond the interface (about 3 mm and 4 mm for the 0.7 and 2 months respectively which correspond to the degraded zone. This zone is linked to the portlandite depleted zone according to XRD results Fig. 7. Note that it is more obvious to distinguish the degraded zone from the sound zone for the 0.7 month sample than that of 2 months. It could be imagined that the crust formation limits degradation and delayed hydration occurs in the degraded zone if the saturated system is closed.

3.2.2. *Chemical and mechanical evolution from the mortar-seawater interface to the internal domain (sound zone) of cast samples*

SEM-EDS analysis was performed on the RHUM sample from the mortar-seawater interface to the sound zone. Results are presented in Fig. 9. The Ca intensity ratio shows three main zones typical of aqueous carbonation of cementitious matrix. At the interface, there is a crust of calcium followed by a highly Ca-depleted zone. The calcium crust size is about 75 μm. This crust is related to aragonite at the interface as shown by XRD results (Fig. 7) and secondary electron image (Fig. 9a). Further in the material, the intensity of the Ca signal increases progressively from the Ca-depleted zone towards the sound zone of the mortar. It is a gradual decalcification from the surface in contact with seawater towards the material sound zone. Mg intensity ratio shows a magnesium crust (about 225 μm) larger than that of calcium. The Mg layer is in line with the brucite as shown by XRD result (Fig. 7) and secondary electron image (Fig. 9c). Si and Al intensity ratio seems to show that the Ca and Mg crusts did not precipitate in the mortar but at the mortar-seawater interface.

Nano indentation was performed on the crust and the sound zone. The results presented on Fig. 9d show on the left the Young's modulus of the aragonite + brucite crust. The crust is mechanically strong (about 60 GPa) against 12 GPa of Young's modulus for the mortar matrix. As shown in Fig. 8b the Ca-depleted zone is low in density and then with high porosity. Nanoindentation tests conducted on this zone failed, likely due to its rugosity.

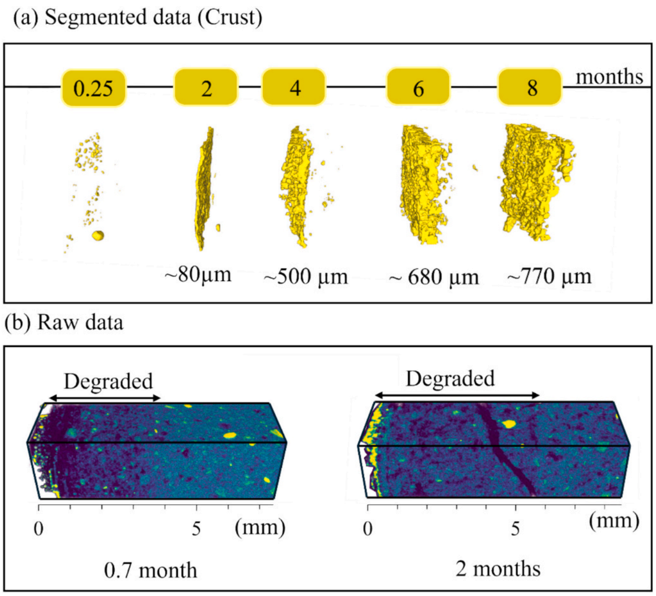

Fig. 8. Microtomography computed images on a RHUM sample at 0.25, 0.7, 2, 4, 6 and 8 months of exposure to seawater: (a) Segmented data of the crust showing its increasing in size with time. (b) Raw data showing different zones from the mortar-seawater interface to the internal domain (sound zone).

4. Discussion

4.1. *Reactive transport modeling of hydration mechanisms in roman underwater concrete*

4.1.1. *Mineralogical and porous water chemistry evolution during hydration*

According to the modeling presented in Fig. 10 and focusing on the evolution of the main minerals, dissolution and precipitation reactions occur simultaneously. At the initial state the portlandite is in equilibrium at pH = 12.45 with 20 mmol/l for calcium concentration (Fig. 10a). When pozzolan is added to the system, its incongruent dissolution releases K^+, SiO_4^{4-}, Al^{3+}, and Na^+ ions into the pore solution, in line with the simulated evolution of these ions, Fig. 10 (c), (d), (e). The release of potassium, silicium and sodium during dissolution of volcanic ash (pozzolan) components agrees with previous study [5]. With these chemical changes, the solubility of C-(A)-S-H is reached, and it precipitates consuming calcium in solution, increasing portlandite dissolution (Fig. 10h). The amorphous pozzolan reactivity was described to fit the experimental data on porewater composition evolution during the hydration mechanism, following the kinetic rate law presented in (Eq. (4)). Note that pozzolan dissolution rate decreases very quickly.

Our modeling results predict the formation of C-(A)-S-H, ettringite, and Friedel salt. The presence of C-(A)-S-H and ettringite agree with the XRD results. There is no thermodynamic data available on hydrocalumite. This gap presents an interesting research avenue for the scientific community. Friedel salt was then used to simulate hydrocalumite precipitation found with XRD as these minerals are quite similar.

The extrapolation of model predicts that all portlandite will be consumed later, and the C-(A)-S-H of high Ca/Si ratio will continue to react with amorphous pozzolan to form a mix of C-S-H and C-A-S-H of low Ca/Si ratio (with an average close to 1.2). The exact composition of this solid phase should be further studied, due to the limited thermodynamic data on C-A-S-H phases. The evolution of porewater chemistry and associated mineralogy are thus in line with the characterizations of the B19 sample, displayed by dashed lines in Fig. 10.

4.1.2. *Mineralogical evolution from the mortar-seawater interface (surface) to the internal domain (sound zone) of cast samples*

The XRD and EDS analyses of the RHUM sample, shown in Fig. 7 and Fig. 9 respectively, revealed carbonation, magnesium and sulfate enrichment at the seawater-mortar interface. These phenomena result from the interaction between HCO_3^-, Mg^{2+} and SO_4^{2-} ions from seawater, and Ca^{2+} and Al^{3+} ions from mortar. Portlandite and gibbsite (representative of an amorphous source of aluminum) are then used to simplify the mortar in RHUM simulation. The results are presented in Fig. 11. Several reactions took place at the seawater-mortar interface during the hydration. Portlandite at the surface dissolves due to the low pH of seawater (pH = 8.2). The Ca^{2+} resulting from this dissolution reacts with seawater carbonate to form calcium carbonate (aragonite) at seawater-mortar interface. This layer is followed by a deeper layer of brucite resulting from the reaction between seawater Mg^{2+} and OH^- (from portlandite dissolution and present in the pore solution). Further sulfate enrichment from seawater lead to ettringite and gypsum precipitation. These successive layers of calcium carbonate, brucite and ettringite agree with the zonation found by Jakobsen et al. in marine concrete [82].

The successive mineralogical fronts simulated here (Fig. 11) agree with SEM-EDS chemical evolution (Fig. 9) and XRD analyses (Fig. 7). However, XRD analyses did not show precipitation of gypsum. Not shown here, XRD analysis was performed on seawater-portlandite sample interface. The experimentation was carried out as done for RHUM sample without pozzolan. It was shown the precipitation of

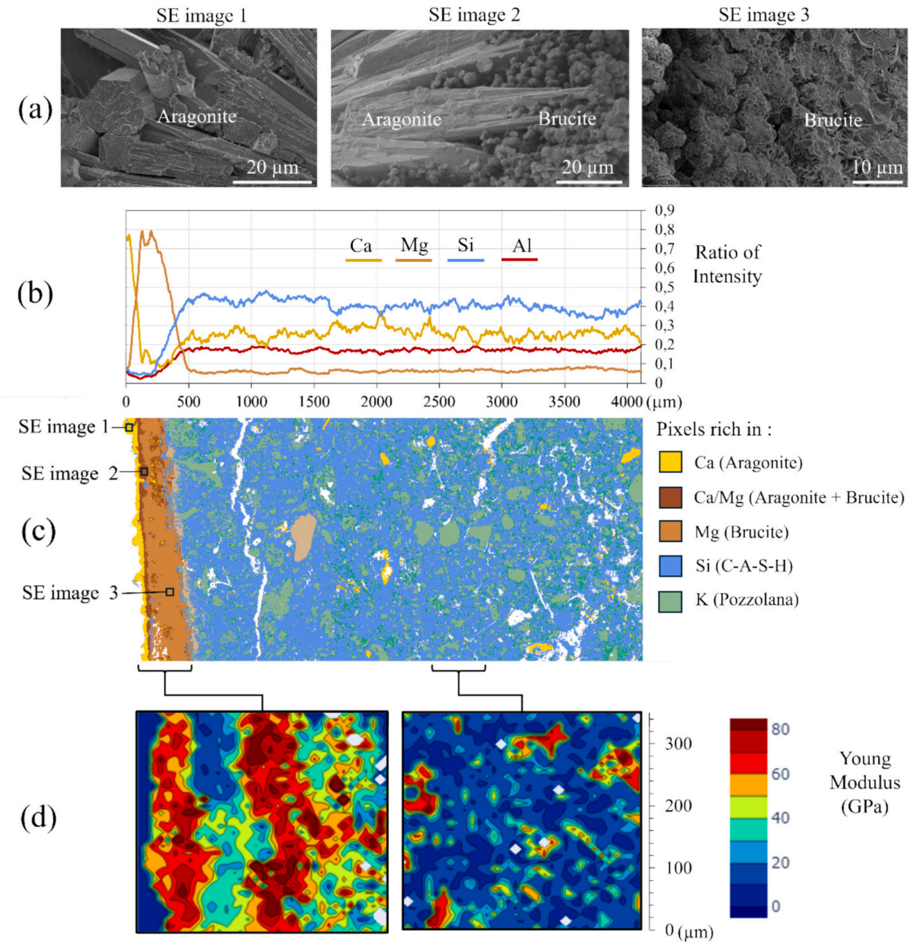

Fig. 9. (a) Secondary electron (SE) image of the interface showing aragonite and brucite at the interface. (b) Ca, Mg, Si and Al intensity ratios built from the EDS map on the matrix (c) from the mortar-seawater interface (surface) to the sound zone of the RHUM sample after 63 days. (d) Nano indentation results on the crust on the left and on the sound zone on the right showing that the crust is mechanically strong.

gypsum in contrast with RHUM sample. The reason for that may be the aluminum released by the dissolution of pozzolan favors ettringite precipitation to the detriment of gypsum.

The simulated porosity evolution from the mortar-seawater interface shows a decrease in porosity due to precipitation of new-minerals, in line with the increased relative density of the crust found with microtomography presented in Fig. 8. Just near the sound zone, the porosity increased due to portlandite dissolution on the one hand and due to the absence of neoformed phases on the other hand. Accordingly, the relative density of the corresponding zone on Fig. 8 decreased. Note that the porosity decrease due to neoformed minerals reduces diffusion process while hydration progresses in the sound zone. According to the parameters chosen for modeling, the effective diffusion coefficient of the crust (brucite + carbonate layer) is lower than that of the sound zone.

4.2. Roman underwater concretes as low-pH cementitious materials

Previous studies on Brindisi replicated roman concrete conducted by ROMACONS project at 6, 42 and 60 months of curing [83,84] have shown the presence of portlandite. In our study, XRD did not indicate the presence of portlandite in the Brindisi 19-year-old matrix (B19). This agrees with the low pH = 12.2 of its pore solution instead of 12.5 when portlandite controls the pH. Furthermore, EDS analysis has indicated Ca/Si = 1.2 for B19 matrix instead of 1.6 when the matrix is in equilibrium with portlandite. The low pH and Ca/Si ratio of B19 are like those of low-pH cementitious materials [24,85]. The diffraction pattern of B19 is relatively similar with that of a low-pH (T3 sample made with 20 wt% of Portland cement, 50 wt% of silica fume and 30 wt% of fly ashes [24]), as presented in Fig. 12. The reason for their similarity is the low Ca/Si ratio of both systems due to the high silica content. When all portlandite has been consumed through pozzolanic reactions, silica continues to be produced by the pozzolan dissolution and reacts with C-A-S-H to decrease the Ca/Si ratio from 1.6 to 1.2. The transformation of reactive components after portlandite has been fully consumed is described by Jackson et al. [86] as post-pozzolanic reactions. Furthermore, the low pH of 12.2 of B19 pore solution and the low Ca/Si ratio of its matrix agree with Lothenbach et al. [85] who explained that the composition of ancient binders corresponds to a low pH cement rather than a Portland cement. The main difference between B19 and low-pH sample lies in the hydrocalumite present in Brindisi sample. This phase is the result of mineralization of chloride ions due to the seawater [1,6,87]. It was proven that the presence of hydrocalumite increased the earlier hardening when seawater is added to lime-pozzolan system [88].

Previous studies [49,89] showed presence of tobermorite and Al-tobermorite in roman maritime concrete from mediterranean harbors. The Brindisi 19 years old pila has been constructed using the same raw materials and the Vitruvius instruction for roman marine structure [10]. However, we did not find these minerals in the B19 sample, potentially highlighting kinetic limitations. Indeed, the pozzolan dissolution will continue in the Brindisi Pila and C-(A)-S-H with a C/S = 1.2 ratio will give way to C-(A)-S-H with a lower C/S ratio (close to 0.8). Then Al-tobermorite will precipitate as preview study [90] on the solubility and characterization of synthesized 11 Å Al-tobermorite proved that it is more stable than poorly ordered C-A-S-H gel.

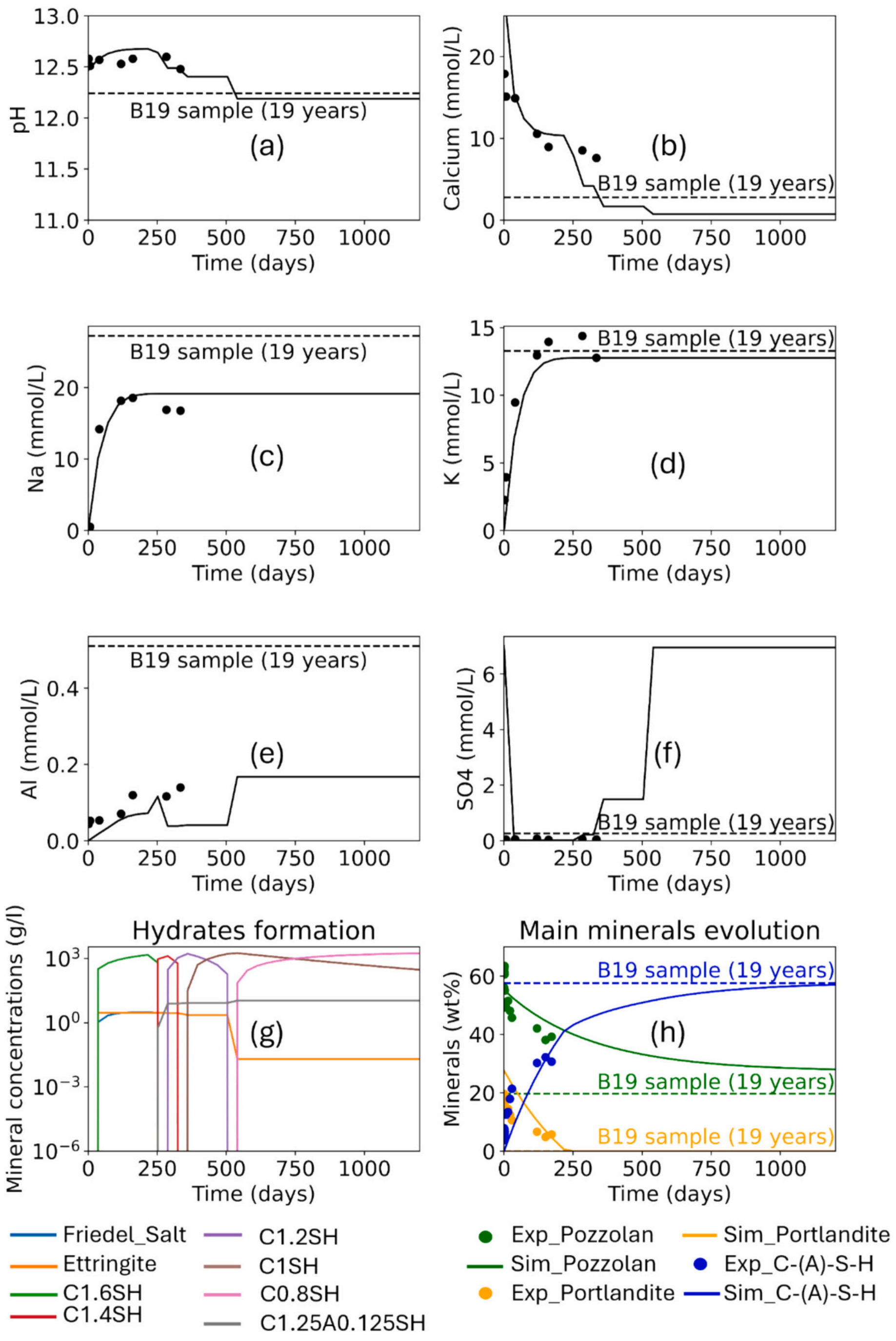

Fig. 10. HYTEC modeling of the mineralogical and porous water chemistry evolution during hydration showing pH and total concentrations of, Ca^{2+}, Na^{+}, K^{+}, Al^{3+} and SO_4^{2-}, and mineralogical evolution. The experimental data are plotted for comparison. The cation concentrations were measured with ICP-OES and that of anions with chromatography. The main mineral evolutions were plotted in wt% with XRD QPA (Rietveld + PONKCS) results presented on Fig. 4. Pozzolan stands for the reactive phase, the amorphous phase of the pozzolan which is the volcanic glass phase of the pozzolan. The dashed lines represent the measured pore water concentration or minerals wt% for the B19 sample.

4.3. Long-term behavior at mortar-seawater interface of roman underwater concretes

Here we link short-term observations at the laboratory scale with those on the Brindisi 19-year-old pila. As done for RHUM sample after 63 days of hydration, XRD were performed on a slice of polished B19 sample from the mortar-seawater interface to the sound zone. The X-Ray diffraction patterns are presented in Fig. 13. Although we cannot claim to have the entire mortar-seawater interface because of the coring procedure, it is quite interesting to compare the successive mineralogical fronts observed on the RHUM sample (Fig. 7) with the Brindisi 19-year-old pila. As shown on RHUM sample, there is a 4 mm mineralogical front characterized by ettringite precipitation at the mortar-seawater interface. It proves that there is sulfate enrichment from seawater. In addition, the M-S-H (magnesium silicate hydrates) presence on the interface until 2.25 mm is related to the interaction between seawater and the pila. However, there is no M-S-H in the RHUM sample after 63 days of hydration (Fig. 7). The magnesium enrichment is characterized by brucite precipitation.

The transition from brucite to M-S-H on the B19 interface remains to

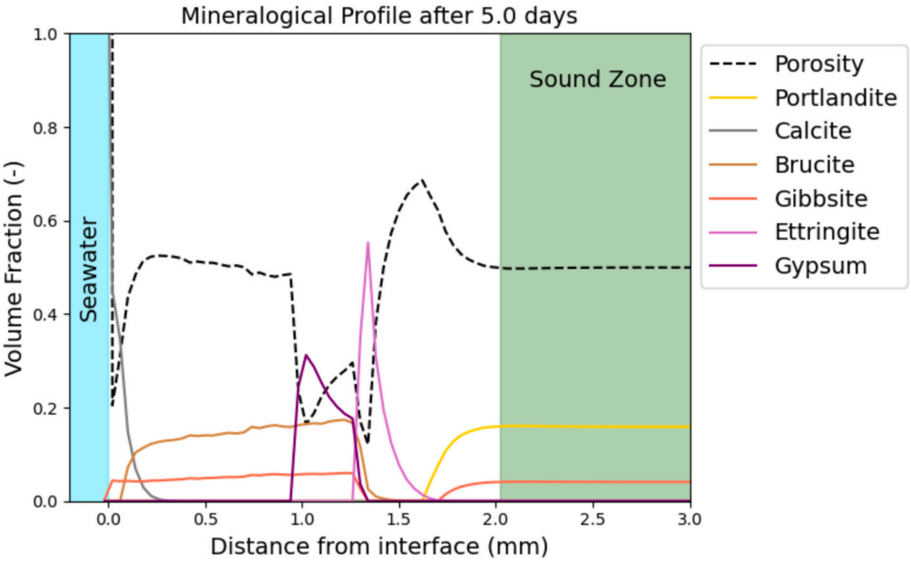

Fig. 11. HYTEC modeling of the mineralogical evolution from the simplified model of mortar-seawater interface (surface) to the sound zone after 5 days of interaction. The saturation indices of M-S-H (magnesium silicate hydrates) phase within the brucite layer of the simulation was positive. Then M-S-H was excluded from the calculation due to its slow formation kinetics under our experimental conditions.

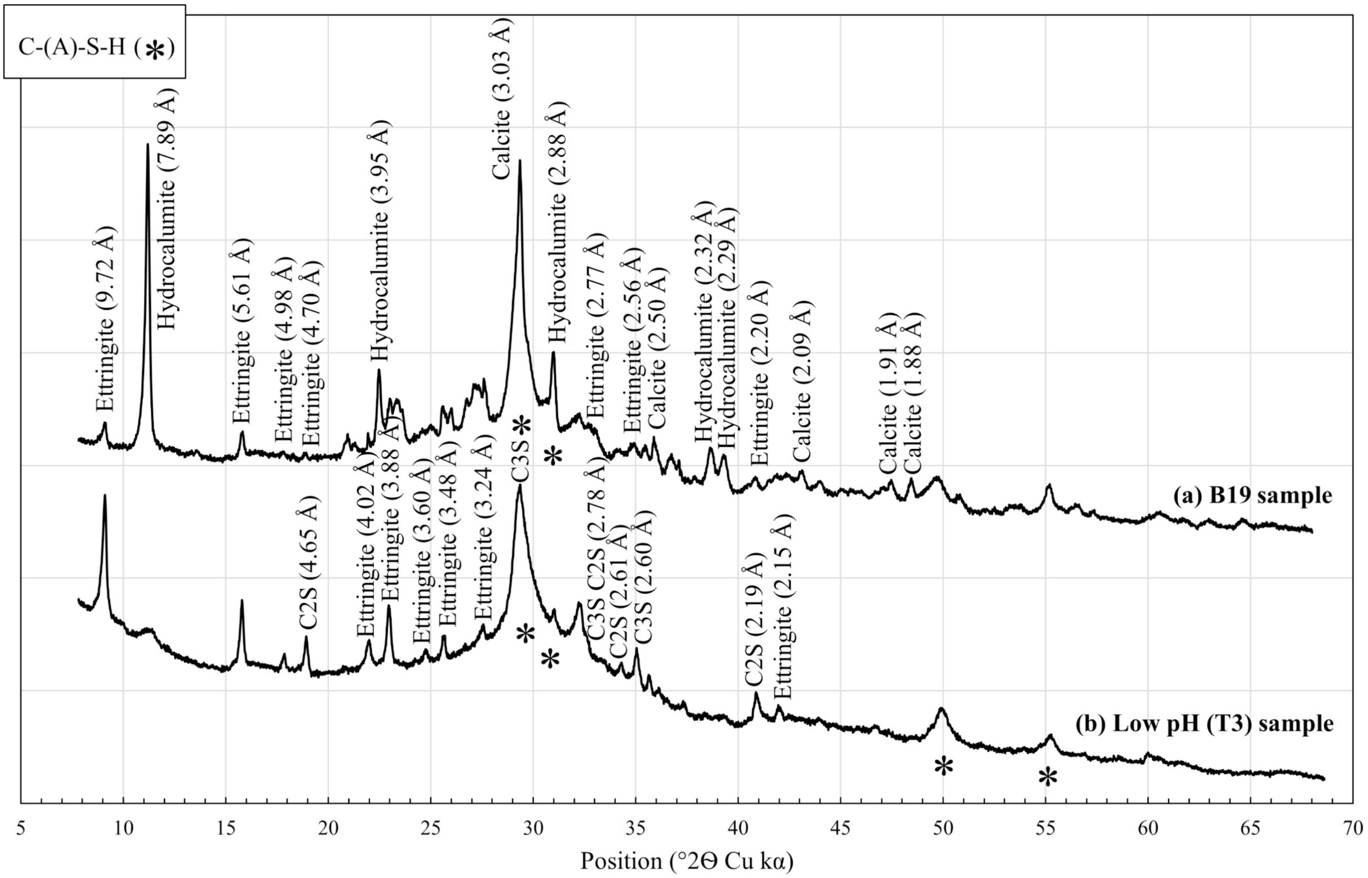

Fig. 12. (a) B19 XRD pattern vs (b) low-pH sample XRD pattern (5 years old hydration) showing the similarity between their mineralogy.

be explained as a previous study on marine concrete showed that where calcium carbonate crust was present on an intact interface M-S-H did not precipitate due to the crust protection [82]. Thus, it could be imagined that the dissolution of amorphous pozzolan, which releases Si, promotes the dissolution of brucite later and the precipitation of M-S-H. Previous studies [91–93] on the reaction process of MgO–SiO_2–H_2O system at room temperature proved that M-S-H formation is generally very slow. These studies showed that a large amount of brucite precipitates in the first days and M-S-H gel are generated progressively until silica or brucite are completely consumed. It was found that the saturation indices of M-S-H phase within the brucite layer of the simulation presented in Fig. 11 were positive, indicating that these phases will

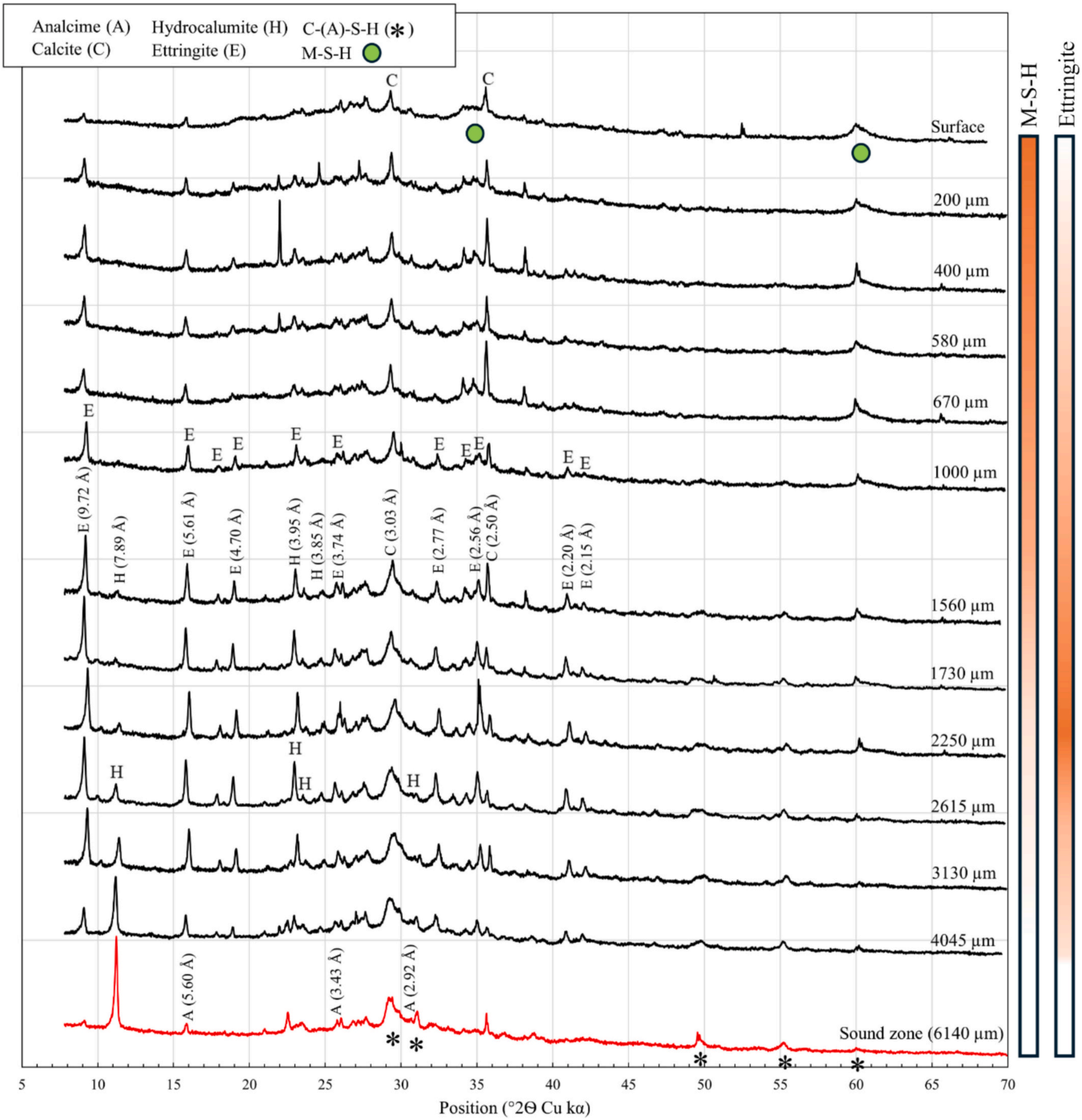

Fig. 13. X-Ray diffraction patterns from the mortar-seawater interface (surface) to the sound zone. XRD tests were performed on a slice of polished B19 sample. Distances are for information only. Colormaps on the right indicate the precipitation extent of M-S-H and ettringite.

eventually replace brucite.

5. Conclusions

This paper studies the hydration mechanisms of underwater roman concrete using pozzolan from the Phlegrean fields, and slaked lime as indicated by Vitruvius. Based on the experimental and 1D reactive transport modeling results hydration mechanism of roman underwater concrete can be summarized in two main phases.

(i) First, when casting roman concrete in seawater as the Romans did 2000 years ago and replicated 19 years ago in the ROMACONS project, Portlandite at the surface dissolves due to the low pH of seawater (pH = 8.2). The Ca^{2+} resulting from this dissolution reacts with seawater carbonate to form calcium carbonate (aragonite) at seawater-mortar interface. This layer is followed by a deeper layer of brucite resulting from the reaction between seawater Mg^{2+} and OH^- (from portlandite dissolution). Further sulfate enrichment from seawater lead to ettringite precipitation. The aragonite + brucite crust with 60 GPa of Young's modulus and its high density decreases the porosity and the diffusion

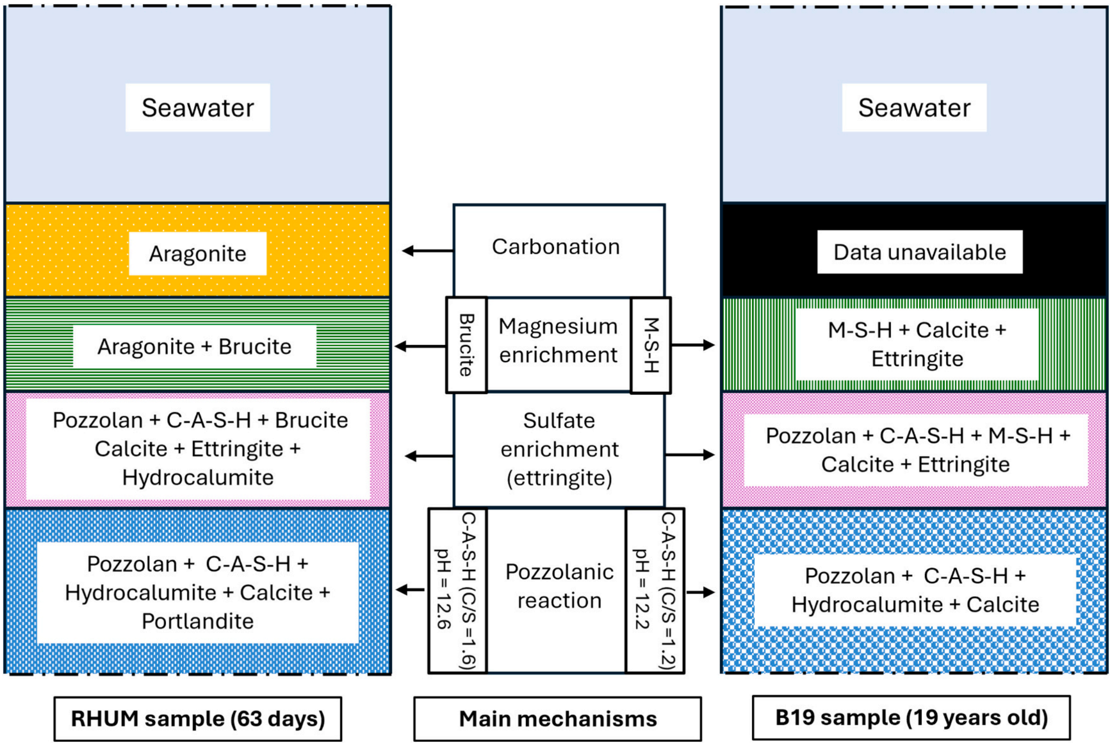

Fig. 14. Main mechanisms of Roman underwater concrete hydration showing at the seawater-mortar interface carbonation, magnesium and sulfate enrichment, and pozzolanic reaction at the sound core. Laboratory replicated sample of 63 days of hydration at the left and at the right the Brindisi 19 years old sample.

process, constituting a diffusive barrier [82,94], allowing hydration processes to continue in the sound zone. With time, the brucite layer will certainly be replaced by the slow precipitation of M-S-H, in agreement with [91].

(ii) The amorphous pozzolan reacts with portlandite to form mainly C-A-S-H which is the matrix binding phase. Other phases such as hydrocalumite and ettringite form [1]. Note that non-reacted pozzolan remain after the complete reaction of portlandite due to the high amount of pozzolan in the system (2 volumes of pozzolan for 1 of lime following Vitruvius instructions for roman maritime structure). Therefore, the C-A-S-H phase continues to incorporate silica as pozzolan dissolution proceeds under the alkaline pH. This leads to a decrease in the Ca/Si ratio from 1.6 to those of low-pH concrete (about 1.2) with 12 GPa of Young's modulus. Calcium concentration decreases with hydration time (from 18 mmol/l after 1 day of hydration to 9 mmol/l after 283 days and reach 2.8 mmol/l after 19 years). The pH seems to be constant around 12.6 still 283 days and decreases later to reach 12.2 after 19 years of hydration.

Compared to previous studies [49,89] that demonstrated the presence of tobermorite and Al-tobermorite in Roman maritime concrete from Mediterranean harbors, our study does not show their presence in the Brindisi 19-year old sample [10] probably due to kinetic limitations.

Our results indicate that during hydration of Roman underwater concrete formation of a dense and mechanically strong aragonite-brucite crust isolates the core from an aggressive environment (Fig. 14), resulting in a highly durable Roman underwater concrete that remains unaltered over two millennia under seawater conditions.

Roman seawater mortars share key characteristics with low-pH cementitious matrices and are exposed to multi-ionic attacks such as carbonation, magnesium, and sulfate ingress under saturated conditions, similar to those expected in seal plugs designed for deep geological disposal of radioactive waste. As such, they serve as valuable archaeological analogues for validating long-term ageing and reactive transport models in the context of radioactive waste management. Perspectives of the RoC project intend to simulate the ageing behavior of that concrete after 2000 years in seawater using reactive transport modeling. Simulation results will be compared with experimental data acquired on 2000 years old mortar. This will allow either to validate model and general approach towards long-term prediction or to reveal its potential shortcomings.

CRediT authorship contribution statement

Fructueux Jesugnon Sohounme: Writing – original draft, Methodology, Investigation, Formal analysis, Data curation, Conceptualization. **Mejdi Neji:** Writing – review & editing, Validation, Supervision, Project administration, Methodology, Funding acquisition, Data curation, Conceptualization. **Nicolas Seigneur:** Writing – review & editing, Validation, Supervision, Project administration, Methodology, Formal analysis, Data curation, Conceptualization. **Katia Schörle:** Writing – review & editing, Validation, Supervision, Project administration, Funding acquisition. **Arnaud Coutelas:** Writing – review & editing, Validation, Supervision, Project administration, Funding acquisition. **T. Charpentier:** Validation, Formal analysis, Data curation. **Mélanie Moskura:** Software, Data curation. **Cyrielle Jardin:** Validation, Formal analysis, Data curation. **Alexandre Dauzères:** Writing – review & editing, Validation, Supervision, Resources, Project administration, Methodology, Investigation, Funding acquisition, Conceptualization.

Declaration of competing interest

The authors declare that they have no known competing financial interests or personal relationships that could have appeared to influence the work reported in this paper.

Data availability

Data are available on the link provided in the manuscript :

https://www.data.gouv.fr/fr/datasets/data-of-article-hydration-mechanisms-in-roman-seawater-concrete/.

Acknowledgments

We are grateful to the ROMACONS team especially to John P. Oleson, Brandon Chris, Robert L. Hohlfelder, L. Bottalico, R. Cucitore, E. Gotti for making a major contribution to our knowledge of Roman mortar, for building the Brindisi pila from which cores were extracted for the RoC project. Our deep appreciation goes to Marcello Molfetta from Italcementi for his support during the extraction cores from the pila in the marina of Brindisi. We are also grateful to Saint Astier for providing the lime putty used in this study. Finally, we extend our thanks to Raphaël Rouyer for his valuable input at the genesis of this project.

References

[1] C.J. Brandon, R.L. Hohlfelder, M.D. Jackson, J.P. Oleson, Building for eternity: the history and technology of Roman concrete engineering in the sea, Oxbow Books, Oxford, 2014.

[2] M. Secco, Y. Asscher, G. Ricci, S. Tamburini, N. Preto, J. Sharvit, G. Artioli, Cementation processes of Roman pozzolanic binders from Caesarea Maritima (Israel), Construct. Build Mater. 355 (2022) 129128, https://doi.org/10.1016/j.conbuildmat.2022.129128.

[3] L. Medeghini, L. Calzolari, M. Botticelli, M. Di Fazio, C. De Vito, I. Pettiti, F. Bardelli, S. Mignardi, The secret of ancient Roman hydraulic mortar: the lesson learnt from the past for future cements, Cem. Concr. Compos. 148 (2024) 105484, https://doi.org/10.1016/j.cemconcomp.2024.105484.

[4] S. Dilaria, G. Ricci, M. Secco, C. Beltrame, E. Costa, T. Giovanardi, J. Bonetto, G. Artioli, Vitruvian binders in Venice: first evidence of Phlegraean pozzolans in an underwater Roman construction in the Venice Lagoon, PloS One 19 (2024) e0313917, https://doi.org/10.1371/journal.pone.0313917.

[5] M.D. Jackson, S.R. Mulcahy, H. Chen, Y. Li, Q. Li, P. Cappelletti, H.-R. Wenk, Phillipsite and Al-tobermorite mineral cements produced through low-temperature water-rock reactions in Roman marine concrete, Am. Mineral. 102 (2017) 1435–1450, https://doi.org/10.2138/am-2017-5993CCBY.

[6] M.D. Jackson, S.R. Chae, S.R. Mulcahy, C. Meral, R. Taylor, P. Li, A.-H. Emwas, J. Moon, S. Yoon, G. Vola, H.-R. Wenk, P.J.M. Monteiro, Unlocking the secrets of Al-tobermorite in Roman seawater concrete, Am. Mineral. 98 (2013) 1669–1687, https://doi.org/10.2138/am.2013.4484.

[7] M.H. Morgan, H.L. Warren, Vitruvius, The Ten Books on Architecture, Cambridge Harvard University Press, London, UK, 1914.

[8] C. Brandon, R.L. Hohlfelder, J.P. Oleson, C. Stern, The roman maritime concrete study (ROMACONS): the harbour of Chersonisos in Crete and its Italian connection, Méditerranée, Revue Géographique Des Pays Méditerranéens / J. Mediterr. Geogr. (2005) 25–29, https://doi.org/10.4000/mediterranee.1952.

[9] P.A. Gianfrotta, Comments concerning recent fieldwork on roman maritime concrete: NOTES, Int. J. Naut. Archaeol. 40 (2011) 188–193, https://doi.org/10.1111/j.1095-9270.2010.00305.x.

[10] J.P. Oleson, L. Bottalico, C. Brandon, R. Cucitore, E. Gotti, R.L. Hohlfelder, Reproducing a Roman maritime structure with Vitruvian pozzolanic concrete, J. Roman Archaeol. 19 (2006) 29–52, https://doi.org/10.1017/S1047759400006255.

[11] H. Goldsworthy, M. Zhu, Mortar studies towards the replication of Roman concrete, Archaeometry 51 (2009) 932–946, https://doi.org/10.1111/j.1475-4754.2009.00450.x.

[12] E. Gotti, J.P. Oleson, L. Bottalico, C. Brandon, R. Cucitore, R.L. Hohlfelder, A comparison of the chemical and engineering characteristics of ancient roman hydraulic concrete with a modern reproduction of vitruvian hydraulic concrete*, Archaeometry 50 (2008) 576–590, https://doi.org/10.1111/j.1475-4754.2007.00371.x.

[13] B. Ma, J.L. Provis, D. Wang, G. Kosakowski, The essential role of cement-based materials in a radioactive waste repository, Npj Mater. Sustain. 2 (2024) 21, https://doi.org/10.1038/s44296-024-00025-9.

[14] P. Perez-Cortes, I. Garcia-Lodeiro, F. Puertas, M.C. Alonso, Effect of incorporating a molten salt waste from nuclear power plants on the properties of geopolymers and Portland cement wasteforms, Cem. Concr. Compos. 142 (2023) 105210, https://doi.org/10.1016/j.cemconcomp.2023.105210.

[15] J. Li, L. Chen, J. Wang, Solidification of radioactive wastes by cement-based materials, Prog. Nucl. Energy 141 (2021) 103957, https://doi.org/10.1016/j.pnucene.2021.103957.

[16] J. Koťátková, J. Zatloukal, P. Reiterman, K. Kolář, Concrete and cement composites used for radioactive waste deposition, J. Environ. Radioact. 178–179 (2017) 147–155, https://doi.org/10.1016/j.jenvrad.2017.08.012.

[17] C. Cau Dit Coumes, S. Courtois, D. Nectoux, S. Leclercq, X. Bourbon, Formulating a low-alkalinity, high-resistance and low-heat concrete for radioactive waste repositories, Cem. Concr. Res. 36 (2006) 2152–2163, https://doi.org/10.1016/j.cemconres.2006.10.005.

[18] M. Atkins, F.P. Glasser, Application of portland cement-based materials to radioactive waste immobilization, Waste Manag. 12 (1992) 105–131, https://doi.org/10.1016/0956-053X(92)90044-J.

[19] M. Alonso, J. Vaunat, M.-N. Vu, J. Talandier, S. Olivella, A. Gens, Three-dimensional modelling of a large-diameter sealing concept in a deep geological radioactive waste disposal, Rock Mech. Rock. Eng. 57 (2024) 4133–4158, https://doi.org/10.1007/s00603-024-03813-w.

[20] N. Chapman, A. Hooper, The disposal of radioactive wastes underground, Proc. Geol. Assoc. 123 (2012) 46–63, https://doi.org/10.1016/j.pgeola.2011.10.001.

[21] S. Liu, S. Chang, Y. Tu, S. Luo, Immobilisation mechanism for nuclear waste containing aluminium by supersulfated cement containing phosphogypsum, Cem. Concr. Compos. 139 (2023) 104991, https://doi.org/10.1016/j.cemconcomp.2023.104991.

[22] D. Jacques, Q.T. Phung, J. Perko, S.C. Seetharam, N. Maes, S. Liu, L. Yu, B. Rogiers, E. Laloy, Towards a scientific-based assessment of long-term durability and performance of cementitious materials for radioactive waste conditioning and disposal, J. Nucl. Mater. 557 (2021) 153201, https://doi.org/10.1016/j.jnucmat.2021.153201.

[23] A. Dauzeres, P. Le Bescop, P. Sardini, C. Cau Dit Coumes, Physico-chemical investigation of clayey/cement-based materials interaction in the context of geological waste disposal: experimental approach and results, Cem. Concr. Res. 40 (2010) 1327–1340, https://doi.org/10.1016/j.cemconres.2010.03.015.

[24] J.L. García Calvo, A. Hidalgo, C. Alonso, L. Fernández Luco, Development of low-pH cementitious materials for HLRW repositories: resistance against ground waters aggression, Cem. Concr. Res. 40 (2010) 1290–1297, https://doi.org/10.1016/j.cemconres.2009.11.008.

[25] M. Xie, D. Su, K.U. Mayer, K.T.B. MacQuarrie, Reactive transport investigations of the long-term geochemical evolution of a multibarrier system including bentonite, low-alkali concrete and host rock, Appl. Geochem. 143 (2022) 105385, https://doi.org/10.1016/j.apgeochem.2022.105385.

[26] P. Lalan, A. Dauzères, L. De Windt, J. Sammaljärvi, D. Bartier, I. Techer, V. Detilleux, M. Siitari-Kauppi, Mineralogical and microstructural evolution of Portland cement paste/argillite interfaces at 70 °C – Considerations for diffusion and porosity properties, Cem. Concr. Res. 115 (2019) 414–425, https://doi.org/10.1016/j.cemconres.2018.09.018.

[27] T. Bach, I. Pochard, C. Cau-dit-Coumes, C. Mercier, A. Nonat, Prediction of long-term chemical evolution of a low-pH cement designed for underground radioactive waste repositories, in: F. Bart, C. Cau-di-Coumes, F. Frizon, S. Lorente (Eds.), Cement-Based Materials for Nuclear Waste Storage, Springer, New York, NY, 2013, pp. 239–249, https://doi.org/10.1007/978-1-4614-3445-0_21.

[28] L. Trotignon, V. Devallois, H. Peycelon, C. Tiffreau, X. Bourbon, Predicting the long term durability of concrete engineered barriers in a geological repository for radioactive waste, Phys. Chem. Earth, Parts A/B/C 32 (2007) 259–274, https://doi.org/10.1016/j.pce.2006.02.049.

[29] U.R. Berner, Evolution of pore water chemistry during degradation of cement in a radioactive waste repository environment, Waste Manag. 12 (1992) 201–219, https://doi.org/10.1016/0956-053X(92)90049-O.

[30] F. Rassineux, J.C. Petit, A. Meunier, Ancient analogues of modern cement: calcium hydrosilicates in mortars and concretes from Gallo–Roman thermal baths of Western France, J. Am. Ceram. Soc. 72 (1989) 1026–1032, https://doi.org/10.1111/j.1151-2916.1989.tb06263.x.

[31] D. Neff, M. Saheb, J. Monnier, S. Perrin, M. Descostes, V. L'Hostis, D. Crusset, A. Millard, P. Dillmann, A review of the archaeological analogue approaches to predict the long-term corrosion behaviour of carbon steel overpack and reinforced concrete structures in the French disposal systems, J. Nucl. Mater. 402 (2010) 196–205, https://doi.org/10.1016/j.jnucmat.2010.05.003.

[32] J.-C. Petit, Natural analogues for the design and performance assessment of radioactive waste forms: a review, J. Geochem. Explor. 46 (1992) 1–33, https://doi.org/10.1016/0375-6742(92)90099-T.

[33] J. van der Lee, L. De Windt, V. Lagneau, P. Goblet, Module-oriented modeling of reactive transport with HYTEC, Comput. Geosci. 29 (2003) 265–275, https://doi.org/10.1016/S0098-3004(03)00004-9.

[34] A. Allahverdi, M. Mahdavan, Durability Performance of RFCC Spent Catalyst-blended Portland Cement Paste Exposed to Sea Water Attack, 2013.

[35] N. Mijatović, A. Terzić, L. Pezo, L. Miličić, D. Živojinović, Validation of energy-dispersive X-ray fluorescence procedure for determination of major and trace elements present in the cement based composites, Spectrochim. Acta B At. Spectrosc. 162 (2019) 105729, https://doi.org/10.1016/j.sab.2019.105729.

[36] D.P. Bentz, P.E. Stutzman, C. Haecker, S. Remond, SEM/X-Ray Imaging of Cement-Based Materials. https://www.nist.gov/publications/semx-ray-imaging-cement-based-materials, 1999. (Accessed 22 July 2021).

[37] R. Castaing, Electron probe microanalysis, in: Advances in Electronics and Electron Physics, Elsevier, 1960, pp. 317–386.

[38] Z. Zhang, J. Qin, Z. Ma, X. Pang, Y. Zhou, Comparison of three different deconvolution methods for analyzing nanoindentation test data of hydrated cement paste, Cem. Concr. Compos. 138 (2023) 104990, https://doi.org/10.1016/j.cemconcomp.2023.104990.

[39] M. Liu, D. Liu, P. Qiao, L. Sun, Characterization of microstructural damage evolution of freeze-thawed shotcrete by an integrative micro-CT and nanoindentation statistical approach, Cem. Concr. Compos. 117 (2021) 103909, https://doi.org/10.1016/j.cemconcomp.2020.103909.

[40] C. Fraley, Algorithms for model-based Gaussian hierarchical clustering, SIAM J. Sci. Comput. 20 (1998) 270–281, https://doi.org/10.1137/S1064827596311451.

[41] E. Patel, D.S. Kushwaha, Clustering cloud workloads: k-means vs Gaussian mixture model, Procedia Comput. Sci. 171 (2020) 158–167, https://doi.org/10.1016/j.procs.2020.04.017.

[42] C. Yuan, H. Yang, Research on k-value selection method of k-means clustering algorithm, J 2 (2019) 226–235, https://doi.org/10.3390/j2020016.

[43] C. Dewitte, L. Lacarrière, M. Neji, A. Bertron, A. Dauzères, Chemo-mechanical characterization of a low-pH model cement paste in magnesium bearing environment, Cem. Concr. Res. 184 (2024) 107598, https://doi.org/10.1016/j.cemconres.2024.107598.

[44] T. Degen, M. Sadki, E. Bron, U. König, G. Nénert, The HighScore suite, Powder Diffract. 29 (2014) S13–S18, https://doi.org/10.1017/S0885715614000840.

[45] K.S. Lothenbach, Ruben Snellings, Chapter 4 - x-ray powder diffraction applied to cement, in: Barbara (Ed.), A Practical Guide to Microstructural Analysis of Cementitious Materials, CRC Press, Boca Raton, 2017, https://doi.org/10.1201/b19074.

[46] X. Li, K.L. Scrivener, Quantification of nano-crystalline C-S-H in hydrated tricalcium silicate, Portland cement and fly ash cement using PONKCS method, Cem. Concr. Res. 191 (2025) 107837, https://doi.org/10.1016/j.cemconres.2025.107837.

[47] C. Naber, S. Stegmeyer, D. Jansen, F. Goetz-Neunhoeffer, J. Neubauer, The PONKCS method applied for time resolved XRD quantification of supplementary cementitious material reactivity in hydrating mixtures with ordinary Portland cement, Construct. Build Mater. 214 (2019) 449–457, https://doi.org/10.1016/j.conbuildmat.2019.04.157.

[48] J.P. Oleson, C. Brandon, S.M. Cramer, R. Cucitore, E. Gotti, R.L. Hohlfelder, The ROMACONS project: a contribution to the historical and engineering analysis of hydraulic concrete in Roman maritime structures, Int. J. Naut. Archaeol. 33 (2004) 199–229, https://doi.org/10.1111/j.1095-9270.2004.00020.x.

[49] G. Vola, M.D. Jackson, J.P. Oleson, C. Brandon, R.L. Hohlfelder, Mineralogical and Petrographic Characterization of Ancient Roman Maritime Concretes from Mediterranean Harbours, Prague, Czech Republic, 2010.

[50] M.D. Jackson, G. Vola, D. Všianský, J.P. Oleson, B.E. Scheetz, C. Brandon, R. L. Hohlfelder, Cement microstructures and durability in ancient Roman seawater concretes, in: J. Válek, J.J. Hughes, C.J.W.P. Groot (Eds.), Historic Mortars, Springer Netherlands, Dordrecht, 2012, pp. 49–76, https://doi.org/10.1007/978-94-007-4635-0_5.

[51] L. Medeghini, L. Calzolari, S. Capriotti, M. Bernabale, C. De Vito, M. Giustini, I. Pettiti, G. Dell'Agli, L. Spiridigliozzi, A. Antonacci, G. Gasperuzzo, V. Scognamiglio, V. Di Tullio, M. Zappelli, L. Conti, E. Gioventù, M. Marcelli, A. Bonaccini, S. Mignardi, How the materials knowledge of Roman mortars could be helpful for the production of future materials: the case of the Aqua Traiana aqueduct (Rome, Italy), Cem. Concr. Res. 179 (2024) 107478, https://doi.org/10.1016/j.cemconres.2024.107478.

[52] E.N. Maslen, V.A. Streltsov, N.R. Streltsova, X-ray study of the electron density in calcite, CaCo3, Acta Cryst. B 49 (1993) 636–641, https://doi.org/10.1107/S0108768193002575.

[53] F. Goetz-Neunhoeffer, J. Neubauer, Refined ettringite (Ca6Al2(SO4)3(OH) 12•26H2O) structure for quantitative X-ray diffraction analysis, Powder Diffract. 21 (2006) 4–11, https://doi.org/10.1154/1.2146207.

[54] D.M. Henderson, H.S. Gutowsky, A nuclear magnetic resonance determination of the hydrogen positions in Ca(OH)21, Am. Mineral. 47 (1962) 1231–1251.

[55] R. Rinaldi, J.J. Pluth, J.V. Smith, Zeolites of the phillipsite family. Refinement of the crystal structures of phillipsite and harmotome, Acta Cryst B 30 (1974) 2426–2433, https://doi.org/10.1107/S0567740874007242.

[56] M. Sacerdoti, E. Passaglia, Hydrocalumite from Latium, Italy: its crystal structure and relationship with related synthetic phases, Neues Jahrb. Mineral. Monatsh. (1988) 462–475.

[57] Dehydration dynamics of analcime by in situ synchrotron powder diffraction, American Mineralogist, GeoScienceWorld, (n.d.). https://pubs.geoscienceworld.org/msa/ammin/article-abstract/84/1-2/112/43491/Dehydration-dynamics-of-analcime-by-in-situ (accessed March 25, 2024).

[58] Crystal-structure refinements of 1M plutonic biotites, American Mineralogist, GeoScienceWorld, (n.d.). https://pubs.geoscienceworld.org/msa/ammin/article-abstract/75/3-4/305/105090/Crystal-structure-refinements-of-1M-plutonic (accessed March 25, 2024).

[59] A.F. Gualtieri, Accuracy of XRPD QPA using the combined Rietveld–RIR method, J. Appl. Cryst. 33 (2000) 267–278, https://doi.org/10.1107/S002188989901643X.

[60] C. Dewitte, Multiphysics evaluation of low CO2 and low pH cementitious matrices exposed to Mg-bearing environments, These de doctorat, INSA, Toulouse, 2023, https://theses.fr/2023ISAT0034 (accessed December 2, 2024).

[61] N. Siddique, S. Paheding, C.P. Elkin, V. Devabhaktuni, U-Net and its variants for medical image segmentation: a review of theory and applications, IEEE Access 9 (2021) 82031–82057, https://doi.org/10.1109/ACCESS.2021.3086020.

[62] Y. Freund, R.E. Schapire, Discussion: arcing classifiers, Ann. Stat. 26 (1998) 824–832.

[63] W.-C. Wang, W.-H. Huang, M.-Y. Lee, H.T.H. Duong, Y.-H. Chang, Standardized procedure of measuring the pH value of cement matrix material by ex-situ leaching method (ESL), Crystals 11 (2021) 436, https://doi.org/10.3390/cryst11040436.

[64] M. Codina, Les bétons bas pH - formulation, caractérisation et étude à long terme, (n.d.).

[65] J. Pouya, M. Neji, L. De Windt, F. Péralès, A. Socié, J. Corvisier, Investigating chemical and cracking processes in cement paste exposed to a low external sulfate attack with emphasis on the contribution of gypsum, Construct. Build Mater. 413 (2024) 134845, https://doi.org/10.1016/j.conbuildmat.2023.134845.

[66] L. De Windt, P. Devillers, Modeling the degradation of Portland cement pastes by biogenic organic acids, Cem. Concr. Res. 40 (2010) 1165–1174, https://doi.org/10.1016/j.cemconres.2010.03.005.

[67] A. Socié, N. Seigneur, B. Bary, S. Poyet, G. Touzé, A fully coupled Hydraulic Mechanical Chemical approach applied to cementitious material damage due to carbonation, Npj Mater. Degrad. 7 (2023) 1–11, https://doi.org/10.1038/s41529-023-00378-x.

[68] N. Seigneur, E. Kangni-Foli, V. Lagneau, A. Dauzères, S. Poyet, P.L. Bescop, E. L'Hôpital, J.-B. d'Espinose de Lacaillerie, Predicting the atmospheric carbonation of cementitious materials using fully coupled two-phase reactive transport modelling, Cem. Concr. Res. 130 (2020) 105966, https://doi.org/10.1016/j.cemconres.2019.105966.

[69] N. Seigneur, K.U. Mayer, C.I. Steefel, Reactive transport in evolving porous media, Rev. Mineral. Geochem. 85 (2019) 197–238, https://doi.org/10.2138/rmg.2019.85.7.

[70] Ph. Blanc, A. Lassin, P. Piantone, M. Azaroual, N. Jacquemet, A. Fabbri, E. C. Gaucher, Thermoddem: a geochemical database focused on low temperature water/rock interactions and waste materials, Appl. Geochem. 27 (2012) 2107–2116, https://doi.org/10.1016/j.apgeochem.2012.06.002.

[71] B. Lothenbach, D.A. Kulik, T. Matschei, M. Balonis, L. Baquerizo, B. Dilnesa, G. D. Miron, R.J. Myers, Cemdata18: a chemical thermodynamic database for hydrated Portland cements and alkali-activated materials, Cem. Concr. Res. 115 (2019) 472–506, https://doi.org/10.1016/j.cemconres.2018.04.018.

[72] K. Shen, X. Qian, C. Hu, F. Wang, Revisiting ancient Roman cement: the environmental-friendly cementitious material using calcium hydroxide-sodium sulfate-calcined clay, ACS Sustain. Chem. Eng. 11 (2023) 5164–5174, https://doi.org/10.1021/acssuschemeng.2c07495.

[73] E. Stora, B. Bary, Q.-C. He, On estimating the effective diffusive properties of hardened cement pastes, Transp. Porous. Med. 73 (2008) 279–295, https://doi.org/10.1007/s11242-007-9170-z.

[74] H. Goldsworthy, M. Zhu, Mortar studies towards the replication of Roman concrete, Archaeometry 51 (2009) 932–946, https://doi.org/10.1111/j.1475-4754.2009.00450.x.

[75] C. Roosz, S. Grangeon, P. Blanc, V. Montouillout, B. Lothenbach, P. Henocq, E. Giffaut, P. Vieillard, S. Gaboreau, Crystal structure of magnesium silicate hydrates (M-S-H): the relation with 2:1 Mg–Si phyllosilicates, Cem. Concr. Res. 73 (2015) 228–237, https://doi.org/10.1016/j.cemconres.2015.03.014.

[76] B. Walkley, J.L. Provis, Solid-state nuclear magnetic resonance spectroscopy of cements, Mater. Today Adv. 1 (2019) 100007, https://doi.org/10.1016/j.mtadv.2019.100007.

[77] G. Paul, E. Boccaleri, L. Buzzi, F. Canonico, D. Gastaldi, Friedel's salt formation in sulfoaluminate cements: a combined XRD and 27 Al MAS NMR study, Cem. Concr. Res. 67 (2015) 93–102, https://doi.org/10.1016/j.cemconres.2014.08.004.

[78] M.D. Andersen, H.J. Jakobsen, J. Skibsted, Characterization of the α−β phase transition in friedels salt ($Ca_2\,Al(OH)_6\,Cl\cdot 2H_2\,O$) by variable-temperature^{27} Al MAS NMR spectroscopy, J. Phys. Chem. A 106 (2002) 6676–6682, https://doi.org/10.1021/jp014573p.

[79] J.A. Chudek, G. Hunter, M.R. Jones, S.N. Scrimgeour, P.C. Hewlett, A.B. Kudryavtsev, Aluminium-27 Solid State NMR Spectroscopic Studies of Chloride Binding in Portland Cement and Blends, (n.d.).

[80] C. Hu, Z. Li, A review on the mechanical properties of cement-based materials measured by nanoindentation, Construct. Build Mater. 90 (2015) 80–90, https://doi.org/10.1016/j.conbuildmat.2015.05.008.

[81] D. Hou, H. Li, L. Zhang, J. Zhang, Nano-scale mechanical properties investigation of C-S-H from hydrated tri-calcium silicate by nano-indentation and molecular dynamics simulation, Construct. Build Mater. 189 (2018) 265–275, https://doi.org/10.1016/j.conbuildmat.2018.08.215.

[82] U.H. Jakobsen, K. De Weerdt, M.R. Geiker, Elemental zonation in marine concrete, Cem. Concr. Res. 85 (2016) 12–27, https://doi.org/10.1016/j.cemconres.2016.02.006.

[83] G. Vola, M.D. Jackson, J.P. Oleson, C. Brandon, R.L. Hohlfelder, Mineralogical and petrographic characterization of ancient Roman maritime concretes from Mediterranean harbours, 2010.

[84] M.D. Jackson, G. Vola, B.E. Scheetz, J.P. Oleson, C. Brandon, R.L. Hohlfelder, Cement Compositions and Durability in Ancient Roman Seawater Concretes, Prague, Czech Republic, 2010.

[85] B. Lothenbach, G. Le Saout, M. Ben Haha, R. Figi, E. Wieland, Hydration of a low-alkali CEM III/B–SiO2 cement (LAC), Cem. Concr. Res. 42 (2012) 410–423, https://doi.org/10.1016/j.cemconres.2011.11.008.

[86] M.D. Jackson, J.P. Oleson, J. Moon, Y. Zhang, H. Chen, M.T. Gudmundsson, Extreme durability in ancient Roman concretes, Am. Ceram. Soc. Bull. 97 (2018) 22–28.

[87] C. Rispoli, Ancient Roman Mortars: Mix Design, Mineralogical Composition and Minerogenetic Secondary Processes, Université de Naples - Frédéric-II, 2017.

[88] W. Ashraf, I.B. Borno, R.I. Khan, S. Siddique, M.I. Haque, A. Tahsin, Mimicking the cementation mechanism of ancient Roman seawater concrete using calcined clays, Appl. Clay Sci. 230 (2022) 106696, https://doi.org/10.1016/j.clay.2022.106696.

[89] M.D. Jackson, J. Moon, E. Gotti, R. Taylor, S.R. Chae, M. Kunz, A.-H. Emwas, C. Meral, P. Guttmann, P. Levitz, H.-R. Wenk, P.J.M. Monteiro, Material and elastic properties of -tobermorite in ancient Roman seawater concrete, J. Am. Ceram. Soc. 96 (2013) 2598–2606, https://doi.org/10.1111/jace.12407.

[90] B. Lothenbach, D. Jansen, Y. Yan, J. Schreiner, Solubility and characterization of synthesized 11 Å Al-tobermorite, Cem. Concr. Res. 159 (2022) 106871, https://doi.org/10.1016/j.cemconres.2022.106871.

[91] E. Bernard, B. Lothenbach, E. L'Hôpital, D. Nied, A. Dauzères, Magnesium Silicate Hydrates (M-S-H): Formation Kinetics and Range of Composition, University of Sheffield, 2014.

[92] Z. Li, T. Zhang, J. Hu, Y. Tang, Y. Niu, J. Wei, Q. Yu, Characterization of reaction products and reaction process of MgO–SiO2–H2O system at room temperature,

Construct. Build Mater. 61 (2014) 252–259, https://doi.org/10.1016/j.conbuildmat.2014.03.004.

[93] T. Zhang, C.R. Cheeseman, L.J. Vandeperre, Development of low pH cement systems forming magnesium silicate hydrate (M-S-H), Cem. Concr. Res. 41 (2011) 439–442, https://doi.org/10.1016/j.cemconres.2011.01.016.

[94] M.L. Conjeaud, Mechanism of Sea Water Attack on Cement Mortar SP 65, 1980, pp. 39–62, https://doi.org/10.14359/6345.